Simulating storm waves in the nearshore area using spectral model: current issues and a pragmatic solution

M. Pezerat, X. Bertin, K. Martins, B. Mengual, L. Hamm

Simulating storm waves in the nearshore area using spectral model: current issues and a pragmatic solution

M. Pezerat[1], X. Bertin[1], K. Martins[2,1], B. Mengual[1], and L. Hamm[3]

[1]UMR 7266 LIENSs, CNRS - La Rochelle Université, 2 rue Olympe de Gouges, 17 000 La Rochelle, France

[2]UMR 5805 EPOC, CNRS - Université de Bordeaux, Allée Geoffroy Saint-Hilaire, F-33615 Pessac, France

[3]ARTELIA, Maritime & Ports branch, 6 rue de Lorraine, 38130 Echirolles, France

Abstract

Short waves are of key importance for nearshore dynamics, particularly under storms, where they contribute to extreme water levels and drive large morphological changes. Therefore, it is crucial to model accurately the propagation and dissipation of storm waves in the nearshore area. In this paper, field observations collected in contrasted environments and conditions are combined with predictions from a third-generation spectral wave model to evaluate four formulations of wave energy dissipation by depth-induced breaking. The results reveal a substantial over-dissipation of incident wave energy occurring over the continental shelf, resulting in a negative bias on significant wave height reaching up to 50%. To overcome this problem, a breaking coefficient dependent of the local bottom slope is introduced within depth-induced breaking models in order to account for the varying degrees of saturation naturally found in breaking and broken waves. This approach strongly reduces the negative bias observed in the shoreface compared to default parameterizations, yielding significant improvements in the prediction of storm waves. Among the implications of this study, our new parameterization of the breaking coefficient results in systematically increased predictions of the wave setup near the shoreline compared to the default parameterization. This increase reaches a factor 2 for gently sloping beaches.

1 Introduction

As storm waves contribute to extreme water levels (Dodet et al., 2019) and drive large morphological changes (Wright and Short, 1984; Coco et al., 2014; Castelle et al., 2015), they are of paramount importance for coastal hazards. In a context of sea-level rise associated with climate change and a continuous increase of coastal populations (Neumann et al., 2015), it is essential to model accurately the propagation, transformation and dissipation of wind-generated surface gravity waves (hereafter short waves) in the nearshore area, in particular during storms.

Regional applications of fully-coupled ocean circulation and spectral wave numerical models have become widespread for all types of applications, ranging from operational predictions to engineering or research purposes (e.g. Bidlot et al., 2002; Boudière et al., 2013; Guérin et al., 2018). However, the ability of these models to accurately simulate wave-induced hydrodynamics during storms in the nearshore area remains uncertain, which is partly explained by the scarcity of field observations required to verify numerical models, especially in the surf zone. In deep water, the parameterizations of the physical processes contributing to wave generation by the wind and its subsequent propagation and transformation have benefited from decades of theoretical and practical developments (e.g. Hasselmann, 1962; Hasselmann and Hasselmann, 1985; The Wamdi Group, 1988; Cavaleri et al., 2007; Ardhuin et al., 2010, and many others). In the nearshore area, dominant processes such as the

adiabatic triad interactions and the dissipation due to depth-induced wave breaking remain heavily parameterized in such models, to the point that the current solutions are sometimes referred to as "engineering solutions" (e.g., see Cavaleri et al., 2007, for a relatively recent review on spectral wave models and the parameterization of the different physical processes involved). Alternatively, modelling chains that combine phase-averaged model forcing local phase-resolving models over a specific area (e.g., see Postacchini et al., 2019) permit to describe the key processes associated with wave transformation in the nearshore while requiring little parameterizations. However, such application remains possible only locally as it is quite computationally expensive, which prohibits this approach for operational applications at the regional scale.

Close to shore, short waves undergo complex transformations and dissipate their energy mostly through depth-induced breaking. In the absence of universal consensus on the criteria for wave breaking and on the spectral distribution of energy dissipation, it is more convenient to model the macroscale effects in terms of the averaged loss of energy. Several formulations have been proposed in the literature to compute the average energy dissipation rate in a Rayleigh-distributed wave field, based on the cross-shore conservation of the bulk wave energy flux. Many of these formulations have subsequently been adapted to compute a corresponding source term for spectral modelling purposes. The underlying approach of depth-induced breaking models follows the seminal work of Le Mehauté (1962), in which the dissipation rate of a breaking (or broken) wave (hereafter referred to as a breaker) is approximated by that of a hydraulic jump of equivalent height (bore-based model). The average energy dissipation rate is obtained by applying the dissipation rate of a breaker to the fraction of breaking (or broken) waves in the original wave field. Therefore, the average energy dissipation rate is controlled by the computation of the fraction of breaking waves (hereinafter Q_b) and a breaking coefficient, which is related to the degree of saturation of the breaker and hence controls its energy dissipation rate. Mostly, the different models differ in the formulation of Q_b and numerous studies further aimed at improving the parameterization of Q_b through *ad hoc* scalings with the local bed slope and/or local wave characteristics (e.g., see Salmon et al., 2015). However, the performance of these scalings remain uncertain at other sites (especially under storm waves) and admittedly lack physical grounds. In contrast, the breaking coefficient has received much less attention in such modelling approach; it is generally kept constant in both time and space, and is seen as a calibration factor. In contrast with these class of depth-induced breaking models, it is worth noting that an alternative approach was proposed by Filipot and Ardhuin (2012). These authors introduced a unified formulation for wave breaking from deep ocean up to the inner surf zone in which a dissipation term is computed for each wave scale based on the decomposition of the frequency spectrum introduced by Filipot et al. (2010). Although this formulation brought interesting insights and showed comparable predictive skills to those specific to deep or shallow water environments, it remains scarcely used especially in studies related to coastal applications.

This study provides a critical and objective assessment of four specialized depth-induced breaking models, which rely on state-of-the-art formulations of the fraction of breaking waves. These models are implemented within the spectral model WWM-III (Roland et al., 2012) fully coupled with a 2DH configuration of the circulation model SCHISM (Zhang et al., 2016). The model performances are assessed at two contrasting sites under high-energy conditions. The results with the default parameterizations show a systematic over-dissipation of the incident wave energy over the inner continental shelf, especially in high-energy conditions. In order to address the inherent limitations of the default parameterizations of these models, which typically consider breakers as fully saturated bores, a new parameterization of the breaking coefficient is introduced based on Le Méhauté's original work (Le Mehauté, 1962).

The manuscript is organised as follows. The theoretical background on depth-induced breaking modelling in parametric models and its application to phase-averaged models is reviewed in Section 2. The two study cases and the model implementation are presented in Section 3. In Section 4, the different depth-induced breaking formulations with their default parameterizations are firstly tested, highlighting their poor predictive skills under high-energy conditions. Then, the performances of the adaptive parameterization of the breaking coefficient within the four models are assessed at the two sites considered here. The results of this study and their implications are discussed in Section 5 before the concluding remarks are provided in Section 6.

2 Theoretical background

2.1 Energy dissipation rate of a broken wave

The analogy between turbulent bores (hydraulic jumps) and individual breakers is often used to compute the associated energy dissipation rate per unit span (D^*) (e.g., see Lubin and Chanson, 2017, for a recent review on these non-linear processes and their similitude). The expression for the energy dissipation rate per unit span by a bore D^*_{bore} is given by Stoker (1957):

$$D^*_{bore} = \rho g Q \frac{(h_0 - h_1)^3}{4 h_1 h_0} = \frac{\rho g}{4} \sqrt{\frac{g(h_0 + h_1)}{2 h_1 h_0}} (h_0 - h_1)^3 \quad (1)$$

where ρ is the water density, g is the gravitational acceleration, Q is the discharge (in m^2/s) and h_0, h_1 are the local water heights upstream and downstream of the discontinuity respectively. Le Mehauté (1962) formulated an analogous expression for breakers (denoted with the subscript wb) by using the discharge given by solitary wave theory. This author further introduced a breaking coefficient, here denoted by δ_{LM}, which is closely related to the fraction of the (active) breaking region over the whole wave face in order to express the energy dissipation rate by a breaker of height H (D^*_{LM}):

$$D^*_{LM} = \delta_{LM} D^*_{wb} \quad (2)$$

$\delta_{LM} = 1$ corresponds to a saturated breaker, where the active, breaking region extends over the whole wave face, while $\delta_{LM} = 0$ corresponds to situations without breaking (Le Mehauté, 1962).

As h_0 and h_1 are *a priori* not known in statistical or phase-averaged numerical models, it is convenient to use the following approximations, introduced by Battjes and Janssen (1978):

$$\begin{cases} h_0 - h_1 & \sim H \\ \sqrt{g \frac{(h_1 + h_0)}{2 h_1 h_0}} & \sim \sqrt{\frac{g}{h}} \end{cases} \quad (3)$$

where h is the mean water depth. When replaced in Eq. 1, these approximations allow to estimate the energy dissipation rate per unit span by a breaker of height H as

$$D^*_{BJ78} \sim \frac{1}{4} \rho g H^3 \sqrt{\frac{g}{h}} = \frac{\alpha}{4} \rho g H^3 \sqrt{\frac{g}{h}} \quad (4)$$

where α is a tuning coefficient of the order of 1 (Battjes and Janssen, 1978). In order to account for the differences in various breaker types and variability in the breaking regime (saturated/non-saturated), Thornton and Guza (1983) proposed the following alternative expression:

$$D^*_{TG83} = \frac{1}{4} \rho g (B H)^3 \sqrt{\frac{g}{h}} \quad (5)$$

Considering the above formulations and approximations used, it is clear that both α and B (hereafter referred to as breaking coefficient) are related to the degree of saturation of the breaker. On the basis of this assessment and considering Le Méhauté's analytical developments, the following expression is introduced as an alternative to Eq. 4 and 5 (see Appendix A for the derivation):

$$D^*_{new} = \frac{B'}{4} \rho g H^3 \sqrt{\frac{g}{h}} \text{ with } B' = 40 \tan\beta \quad (6)$$

where $\tan\beta$ is the local bottom slope. This new formulation incorporates the effect of the bottom slope on the local rate of energy dissipation in a breaker. An illustrative evidence of such dependency can be found in Martins et al. (2018) who performed high resolution measurements of broken waves propagating in the inner surf zone with a lidar scanner (see their Fig. 3). Extracting the breaker properties (height, roller angle and length),

one can notice that beach slope variations yield changes in roller geometrical properties, which subsequently control the rate at which the energy is dissipated. Furthermore, this parameterization is consistent with the bottom slope dependency of the parameter α discussed by Hamm (1995). Although B' can theoretically grow to infinite, it is physically bound to $[0;1]$, which means that the breaker saturation is reached over slopes equal to or steeper than 1:40.

2.2 Total energy dissipation rate of random breaking waves

The original approach to model the transformation of random waves in the nearshore typically assumes the wave field to be Rayleigh-distributed and narrow-banded in both frequency and direction. As only bulk parameters are simulated, the representative period remains constant over space with this approach. On sandy shores, the cross-shore evolution of the wave energy flux is principally controlled by the depth-induced breaking intensity, given by the local mean (period-averaged) rate of energy dissipation per unit area of breaking (or broken) waves D_{br}. This term is computed by dividing the energy dissipation rate per unit span by a breaker (e.g., Eq. 4, 5 or 6) by a representative shallow water wave length $\overline{\lambda} = \sqrt{gh}/\overline{f}$ (where $\overline{f}$ is a representative frequency of the energy spectrum) applied to the fraction of breaking and broken waves of the original wave field.

2.2.1 Battjes and Janssen (1978) model (BJ78)

Battjes and Janssen (1978) assumed that the height of all breakers equals a local maximum possible wave height H_m estimated by means of a parameterized Miche type criterion:

$$H_m = \frac{0.88}{k} \tanh\left(\frac{\gamma k h}{0.88}\right) \tag{7}$$

where k is the wavenumber and γ is the breaking index, an adjustable coefficient to allow for effects of bottom slope compared to the theoretical value of 0.88 given by the Miche criterion derived for a flat bottom (Miche, 1944). In shallow water ($kh \ll 1$), Eq. 7 reduces to:

$$H_m = \gamma h \tag{8}$$

As a result, the Rayleigh's probability density function of wave heights is clipped at $H = H_m$ with a delta function. According to their analytical developments, the fraction of breaking waves Q_b is consequently computed by means of:

$$\frac{1 - Q_b}{-\ln(Q_b)} = \left(\frac{H_{rms}}{H_m}\right)^2 \tag{9}$$

where H_{rms} is the root mean square wave height. Assuming $H_m/h = \mathcal{O}(1)$ where the dissipation occurs, the local mean rate of energy dissipation per unit area finally reads:

$$D_{br,BJ78} = \frac{\alpha}{4} \rho g f_{mean} Q_b H_m^2 \tag{10}$$

where f_{mean} is a mean frequency which is typically computed from the $T_{m0,1}$ wave period (defined as m_0/m_1, see Eq. 23 in Section 3.1.3).

Battjes and Stive (1985) performed an extensive calibration and verification of this model using a variety of experimental and field observations. Although the original model was developed using a mean frequency, it should be pointed out that these authors used the peak frequency f_p instead of f_{mean} in Eq. 10. With the calibration coefficient α kept at 1, the values for the breaking index γ ranged from 0.60 to 0.83 with an average of 0.73 (in the original paper, Battjes and Janssen, 1978, used $\gamma = 0.8$ and $\alpha = 1$). From these results, Battjes and Stive (1985) found a relation between γ and the offshore wave steepness s_o, which was later adjusted by Nairn (1990):

$$\gamma = 0.39 + 0.56 \tanh(33 s_o) \text{ with } s_o = \frac{H_{rms,o}}{\lambda_o} = H_{rms,o} \frac{2\pi f_p^2}{g} \tag{11}$$

2.2.2 Thornton and Guza 1983 model (TG83)

Based on their field observations, Thornton and Guza (1983) suggested that the wave field was also Rayleigh-distributed in the surf zone. These authors expressed the distribution of breaking wave heights $p_b(H)$ as a weighting of the Rayleigh probability density function for all wave heights $P(H)$ by means of a function $W(H)$, such that:

$$Q_b = \int_0^\infty p_b(H)dH = \int_0^\infty W(H)P(H)dH \tag{12}$$

The total energy dissipation is obtained by integrating the energy dissipation for a single broken wave of height H (Eq. 5) multiplied by $p_b(H)$ (Thornton and Guza, 1983). This reads:

$$D_{br,TG83} = \int_0^\infty \frac{f_p}{\sqrt{gh}} D^*_{TG83} W(H)P(H)dH = \frac{B^3}{4}\rho g \frac{f_p}{h}\int_0^\infty H^3 W(H)P(H)dH \tag{13}$$

Two expressions for the weight function were proposed in terms of the ratio H_{rms}/h to fit the observed fraction of breaking waves from a field campaign conducted at Soldiers Beach, California (Thornton and Guza, 1983). This follows Thornton and Guza (1982) who showed the depth-limited character of inner surf zone waves and found a linear relationship between H_{rms} and h. For brevity, the single expression introduced by Battjes and Janssen (2009) is used:

$$W^i_{TG83}(H) = \left[1 - \exp\left(-\left(\frac{H}{\gamma_{TG}h}\right)^2\right)\right]^i \left(\frac{H_{rms}}{\gamma_{TG}h}\right)^{n_i} \tag{14}$$

For $i = 0$, W^0_{TG83} is independent of the wave height, whereas, for $i = 1$ the distribution of broken waves is skewed towards the largest waves (i.e., they are more likely to break). The coefficient γ_{TG} is set to 0.42 according to Thornton and Guza (1982) whereas, depending on the weight function used, the most accurate description of the distribution of breaking waves was obtained using $n_0 = 4$ or $n_1 = 2$. Substituting Eq. 14 for $i \in [\![0, 1]\!]$ in Eq. 13 yields:

$$D^i_{br,TG83} = \frac{3\sqrt{\pi}}{16} B^3 f_p \rho g \frac{H^3_{rms}}{h}\left[1 - \left(1 + \left(\frac{H_{rms}}{\gamma_{TG}h}\right)^2\right)^{-5/2}\right]^i \left(\frac{H_{rms}}{\gamma_{TG}h}\right)^{n_i} \tag{15}$$

The model has only one adjustable parameter B (introduced in Eq. 5), whose optimal values ranged from 0.8 to 1.7 depending on the dataset (whether field or lab-based observations) and the weight function (Thornton and Guza, 1983). Considering that the coefficient is used at power 3, it is worth noting that the resulting value for $D_{br,TG83}$ can vary by up to a factor 10.

2.2.3 Baldock *et al.* 1998 model (B98)

The model originally proposed by Baldock et al. (1998) borrows from BJ78 and TG83 models. It uses a Heavyside step function shifted in H_m to weigh the Rayleigh's probability density function. Janssen and Battjes (2007) reported an inconsistency in the original analytical developments and proposed a corrected expression for the local mean rate of energy dissipation per unit area which reads:

$$D_{br,B98} = \frac{3\sqrt{\pi}}{16}\alpha f_p \rho g \frac{H^3_{rms}}{h}\left[1 + \frac{4}{3\sqrt{\pi}}\left(R^3 + \frac{3R}{2}\right)\exp(-R^2) - \mathrm{erf}(R)\right] \tag{16}$$

where $R = H_m/H_{rms}$, erf is the error function and H_m is computed according to Eq. 8. The formulation based on the offshore wave steepness (Eq. 11) was used in both papers to compute γ.

2.3 Recent developments on the parameterization of Q_b

2.3.1 Alternative parameterizations of the breaking index

A dependency of the breaking index to the local non-dimensional depth was investigated by Ruessink et al. (2003), who introduced a parameterization of γ which linearly increases with the local non-dimensional depth based on the peak period $k_p h$:

$$\gamma = 0.76 k_p h + 0.29 \tag{17}$$

This parameterization is based on the calibration through an inverse modelling approach of a 1D cross-shore bulk wave model in which depth-induced breaking is modelled according to Baldock's original formulation (Baldock et al., 1998). This parameterization of the breaking index has been implemented within spectral models yielding a substantial improvement in model results (van der Westhuysen, 2010). More recently, alternative parameterizations of the breaking index with both local bottom slope and non-dimensional depth were proposed (Salmon et al., 2015; Lin and Sheng, 2017) with a calibration performed with spectral models against extensive datasets. These parameterizations follow earlier experimental studies in which the dependency of the wave height over depth ratio in the inner surf zone to these two parameters was already pointed out (Raubenheimer et al., 1996; Sénéchal et al., 2001).

2.3.2 Westhuysen 2010 model (W10)

van der Westhuysen (2010) further investigated breaker index parameterization based on wavefield nonlinearity and introduced an alternative parameterization of Q_b which relies on the biphase β_i, a third-order quantity that informs on the phase coupling between triads and is thus related to the wave skewness and asymmetry (e.g., see Hasselmann et al., 1963; Elgar and Guza, 1985). As spectral wave models do not represent quantities at this order, β_i is generally approximated from a linear estimate of the Ursell number Ur (Eldeberky, 1997; Doering and Bowen, 1995). Following the approach of Thornton and Guza (1983), the following expression for the weight function W was proposed:

$$W_{W10}(H) = \left(\frac{\beta_i}{\beta_{i,\,ref}}\right)^n \text{ with } \beta_i = -\frac{\pi}{2} + \frac{\pi}{2}\tanh\left(\frac{\delta}{Ur}\right) \tag{18}$$

where $\delta = 0.2$ according to Eldeberky (1997) and Ur is computed with its bulk formulation:

$$Ur = \frac{g}{8\sqrt{2}\pi^2}\frac{H_{m0}T_{m0,1}^2}{h^2} \tag{19}$$

By construction, when $\beta_i = 0$ (i.e. waves are symmetric along the vertical axis) the percent of broken waves equals zero, when β_i tend to $-\frac{\pi}{2}$, waves become more asymmetric (i.e. pitched forward, e.g. see Elgar and Guza, 1985) and the percent of broken waves increases. However, as all waves tend to break before the limit is reached, a scaled limit $\beta_{i,\,ref}$ was introduced in the expression of the weighting function. In the study by van der Westhuysen (2010), the coefficients $\beta_{i,\,ref}$ and n were respectively set to $-4\pi/9$ and 2.5 in order to fit the observed fraction of breakers in the lab experiment of Boers (1996). Using Eq. 5, the local mean rate of energy dissipation per unit area is finally given by:

$$D_{br,W10} = \frac{3\sqrt{\pi}}{16}B^3\rho g\frac{f_{mean}}{h}\left(\frac{\beta_i}{\beta_{i,\,ref}}\right)^n H_{rms}^3 \tag{20}$$

where f_{mean} is the mean frequency computed from the $T_{m0,1}$ wave period. As for the TG83 model, B is the only adjustable parameters. According to van der Westhuysen (2010), it resulted from calibrations that the value of B varied over the range 0.5 to 1.5.

2.4 Depth-induced breaking in spectral models

Spectral wave models are based on a decomposition of the sea surface elevation in a sum of linear components across relative angular frequencies σ and directions θ. These models solve a balance equation for the wave action density spectrum (N), which is related to the wave energy density spectrum (E) by $N = E/\sigma$ (e.g. see Komen et al., 1994):

$$\frac{\partial N}{\partial t} + \nabla_{\boldsymbol{x}} \cdot [(\boldsymbol{C_g} + \boldsymbol{U})N] + \frac{\partial(\dot{\sigma}N)}{\partial \sigma} + \frac{\partial(\dot{\theta}N)}{\partial \theta} = S_{tot} \tag{21}$$

The left-hand side of Eq. 21 contains the change of wave action in time, the advection in the geographical space at a velocity given by the intrinsic group speed vector $\boldsymbol{C_g}$ plus an advective current velocity vector $\boldsymbol{U}$ for each spectral component, which theoretically depends on the current profile (Andrews and McIntyre, 1978) and on the amplitude of all waves components (Willebrand, 1975). In practice, these latter effects are often neglected, such that within numerical models, $\boldsymbol{U}$ is generally taken as the surface current velocity vector or, for coastal applications, the depth-averaged current (Cavaleri et al., 2007). In WWM-III, $\boldsymbol{U}$ is approximated to be the surface current velocity vector (Roland et al., 2012). The last two terms correspond to the advection in spectral space where $\dot{\sigma}$ and $\dot{\theta}$ are the propagation velocities in frequencies and directions respectively.

The evolution of the action spectrum due to a variety of physical phenomena is represented through source terms summed in the right-hand side of Eq. 21. In deep water, wind-driven wave growth (S_{in}), dissipation by whitecapping (S_{ds}) and non-linear quadruplet interactions (S_{nl4}) are the dominant processes transforming the wave field. In shallow water, three additional processes are considered namely the bottom friction (S_{bf}), non-linear interactions between triads (S_{nl3}) and depth-induced breaking (S_{br}).

The main approach to compute the depth-induced breaking source term follows the work of Eldeberky and Battjes (1996) in which the local mean rate of energy dissipation is distributed over frequencies and directions in proportion to the spectral action density:

$$S_{br} = \frac{D_{br}}{E_{tot}} N \text{ where } E_{tot} = \rho g \int_{\sigma} \int_{\theta} E d\sigma' d\theta' \tag{22}$$

Consequently, the aforementioned formulations of the local mean rate of energy dissipation per unit area could be introduced into spectral models. It is worth noting that for the BJ78 and B98 original models, the parameterizations of the breaking index based on offshore wave parameters (Eq. 11, see also Apotsos et al., 2008, who proposed a parameterization with the offshore significant wave height) are not convenient for spectral models applied at regional scale. This contrasts with one-dimensional, smaller-scale models, based on the cross-shore balance of the wave energy flux and which obtained satisfactory results with such parameterizations. Following the approach of the SWAN group (Booij et al., 1999), a constant value of $\gamma = 0.73$ consistent with the results of Battjes and Stive (1985) is usually used to compute H_m by means of Eq. 8.

3 Methods

The present study is supported with field measurements from two study areas: the Oléron Island, France, and Duck, North Carolina. This section presents the two study cases, underlying their contrasting features. The model implementation and the result assessment methodology are subsequently described.

3.1 Study cases

3.1.1 Oléron 2010 (O10)

The first study area is located along the South-West coast of the Oléron Island in the central part of the French Atlantic coast (see Fig. 1a). This area is characterized by a very gently sloping shoreface where the bottom slope is of the order of 1:1000 and a non-barred dissipative beach where bottom slope approximatly reaches 1:100 (Fig. 1c). Tides are semi-diurnal and range from 1.5 m during neap tides to 5.5 m during spring tides, which

corresponds to a macrotidal regime. Dodet et al. (2019) recently analysed wave regimes along the 30 m isobath of the French metropolitan coast. In this area, the yearly mean wave conditions reported are characterized by a significant wave height of 1.6 m, a mean wave period of 5.9 s and a direction of 285° from the true North.

This case study is supported by observations from a field campaign carried out by the French Hydrographic and Oceanographic Office in February 2010. During the studied period, offshore waves were characterized by a significant wave height reaching 9.5 m at Biscay Buoy location which corresponds to a yearly return period (Nicolae-Lerma et al., 2015) while the local wave growth in the nearshore area is negligible due to weak local wind. The dataset includes data from a Datawell buoy (DW) and two pressure sensors (VEC and P3) mounted on a structure dropped on the seabed (see Fig. 1b - 1c for their respective location). The DW wave bulk parameters at the peak of the storm are given in Table 1.

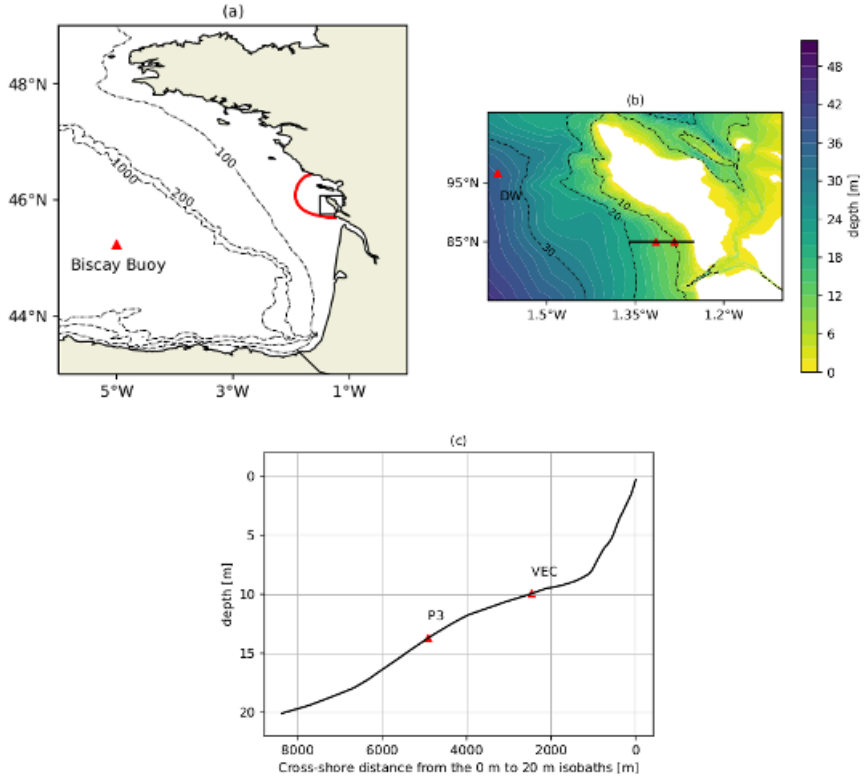

Figure 1: **(a)** Location of the Oléron Island in the Bay of Biscay (black box), limit of the computational domain (red dotted line) and position of the Biscay Buoy (red triangle; lon=5°W, lat=45.23°N). **(b)** Zoom on the study area with the bathymetry reduced to the Mean Sea Level. Red triangles refer to the three sensors used: the DW (lon=−1.5833°W, lat=45.9667°N) was deployed at 33 m depth, while P3 (lon=−1.3150°W, lat=45.8500°N) and VEC (lon=1.2833°W, lat=45.8500°N) were deployed at 13 m and 9 m depth respectively. A cross-shore profile between the 0 m and 20 m isobaths is symbolised with the black line. The profile is plotted in panel **(c)**

3.1.2 Duck 2016 (D16)

The second study area is located on the shoreface surrounding the Field Research Facility (FRF) near Duck, NC (see Fig. 2a). The FRF is maintained by the U.S. Army Corps of Engineers and has focused for many decades the effort of the coastal researcher's community through major field campaigns. In particular, as topographic surveys are being performed regularly and nearshore current, wave and water level data are continuously collected and available to the community, this site often serves as a benchmark for numerical models. Around the FRF, the bottom topography is quite alongshore-uniform (Fig. 2b) and is characterized by a steep foreshore, generally flanked by a flat terrace/sandbar system ($\mathcal{O}(100\,\mathrm{m})$ in length, e.g. see Gallagher et al., 1998), beyond which the slope is gentle and decreases monotonically from 1:200 to 1:1000 (Fig. 2c). As large morphological changes of the sandbar take place under storm waves while we used a fixed bathymetry in this study, only the observations available seaward of the bar are presently considered (i.e. minimum water depth of 3 m).

The D16 case study focuses on high energetic sea states associated with Hurricane Matthew over the period from October the 3rd to the 11th and is supported with data from the FRF database. The dataset includes measurements from a Waverider buoy (WR) in intermediate depth in addition of two other sensors: a pressure sensors array deployed in 8 m depth (AS) and a current profiler deployed in 3.5 m depth (ADOP, Fig. 2b and 2c). The WR wave bulk parameters at the peak of the storm are given in Table 1. In particular, it is stressed that significant wave height reaching approximately 5 m typically occured one or two times per year over the last decade. Furthermore, spectra timeseries (not shown) show a slight contribution of locally generated waves superimposed to the incomming swell during the studied period.

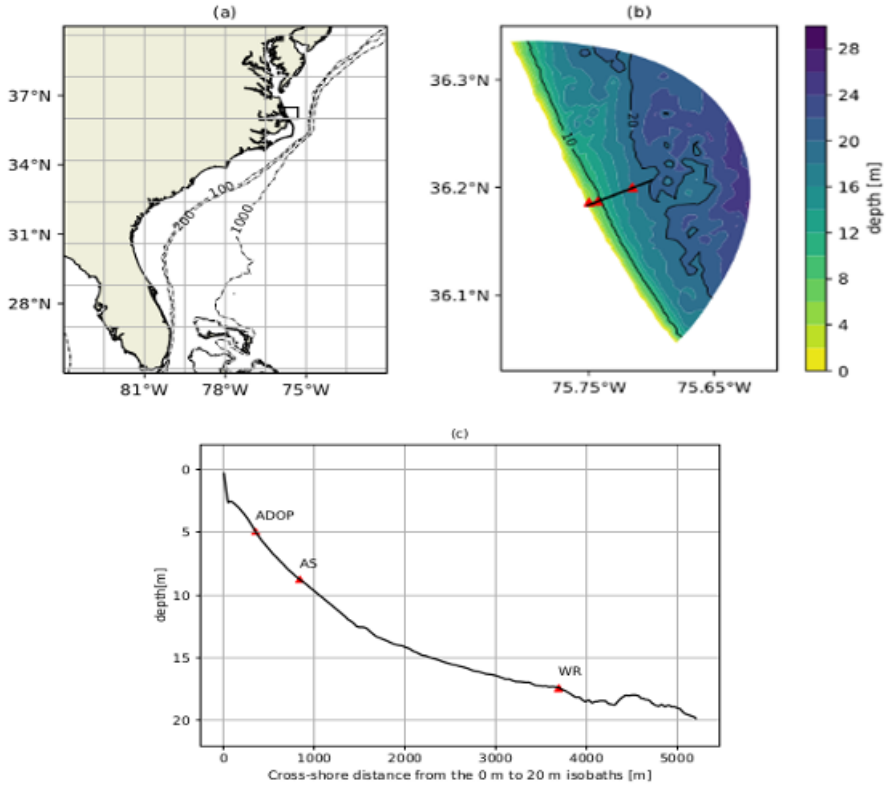

Figure 2: Same as Figure 1 for D16 study case. The geographical coordinates of each sensor are: WR - lon=75.71533°W, lat=36.2002°N; AS - lon=75.7429°W, lat=36.1872°N; ADOP - lon=75.7498°W, lat=36.1865°N.

Study Case	O10	D16
H_{m0}	6.7 m	4.8 m
T_{pc}	16 s	11 s
T_{m02}	12 s	8 s
Peak Direction	273°	110°
Directional Peak Spreading	15°	30°

Table 1: Wave bulk parameters at the peak of the storm at the most seaward sensor of each study case (respectively, the DW and WR buoys).

3.1.3 Computation of bulk parameters

For study case O10, sub-surface pressure timeseries from the two pressure sensors were split into 20 minute-long bursts. Pressure measurements were corrected for sea-level atmospheric pressure and detrended. Then, the free surface elevation signal was reconstructed using the Transfer Function Method based on linear wave theory (TFM, e.g. see Bishop and Donelan, 1987). This method requires an upper cutoff frequency for not correcting and amplifying noise in the pressure data at high frequencies, a problem which increases exponentially with

depth. The cutoff frequency was set to 0.2 Hz for P3 and VEC sensors, which roughly corresponds to an amplification factor up to 50, a value well below the threshold of 100 recommended by Smith (2002). Finally, the sea surface elevation density spectra $E(f)$ were computed by means of a Fast Fourier Transform on 10 Hanning-windowed segments with a 50% overlapping. Elevation spectra were directly obtained from the DW data. Similarly, for study case D16, elevation spectra are directly available for each sensor through the FRF database.

Wave bulk parameters are computed using the p^{th} moments of each spectra defined as:

$$m_p = \int_{f_{min}}^{f_{max}} f^p E(f) df \tag{23}$$

For study case O10, the f_{max} value was chosen in agreement with the upper cutoff frequency used to reconstruct the free surface elevation for the two pressure sensors and it was also set to 0.2 Hz for DW spectra. This conservative cut-off frequency for the DW spectra was constrained by a seemingly unphysical signal at higher frequencies. It was set to 0.3 Hz for every sensors of the D16 study case. Following Roelvink and Stive (1989) or Hamm and Peronnard (1997), an adaptive f_{min} value was defined as half of the continuous peak frequency (f_{pc}) computed at the offshore sensor (DW and WR for study cases O10 and D16, respectively) as:

$$f_{pc} = \frac{m_0^2}{m_{-2} m_1} \tag{24}$$

Finally, the significant wave height and the mean wave period were respectively computed as:

$$H_{m0} = 4\sqrt{m_0} \tag{25}$$

$$T_{m0,2} = \sqrt{\frac{m_0}{m_2}} \tag{26}$$

3.2 Modelling system

The third-generation Wind Wave Model (WWM, Roland et al., 2012) is used within the SCHISM framework (Zhang et al., 2016) to simulate the generation, propagation and transformation of short waves in the nearshore. The full coupling between the 2DH circulation model and the wave model is made at the source code level. The same unstructured mesh and domain decomposition are shared by both models.

For both study cases, the atmospheric forcing consisted of Mean Sea Level pressure and wind speed at 10 m. For the case D16, hourly data originating from the Climate Forecast System Reanalysis (CFSR, Saha et al., 2011) were interpolated on a 0.2° regular grid. For the case O10, the three-hourly data from the Integrated Forecasting System of the European Center for Medium-Range Weather Forecast were used (Owens and Hewson, 2018). These are extracted from a 0.125° regular grid.

At the offshore domain boundaries, WWM was forced with timeseries of energy spectra obtained from a North Atlantic application of the spectral wave model WaveWatch III (WW3, Tolman, 1991). For the case O10, the tidal forcing was computed by considering the 16 main tidal constituents linearly interpolated from the regional tidal model of Bertin et al. (2012). For the case D16, water levels were forced with the measurements from the AS sensor in order to account for the surge that developed at the scale of the whole continental shelf, which is not entirely represented in the computational grid. Thus, atmospheric forcing was switched off for the circulation model. For both WWM and WWIII models, the wind input and dissipation by whitecapping were formulated according to the parameterization of Ardhuin et al. (2010). Non-linear quadruplet interactions were taken into account following the approach of Hasselmann and Hasselmann (1985). In WWM, the non-linear triad interactions were parameterized following Eldeberky's approach (Eldeberky, 1997) and the JONSWAP parameterization for the bottom friction was used with a coefficient $\Gamma = 0.038$ m^2.s^{-3} (Hasselmann et al., 1973). Depth-induced breaking source term was computed following the approach of Eldeberky and Battjes (1996), as described in Section 2.4. Finally, the (θ, σ) space was discretized in 36 directions and 24 frequencies ranging from 0.02 to 0.4 Hz.

3.3 Results assessment

Model results are compared to observations by means of bulk parameters computed with moments integrated over the same frequency range as the data. The results on the significant wave height H_{m0} are the most relevant to assess depth-induced breaking model performances whereas the results on T_{pc} and T_{m02} bring insight, respectively, on the energy peak and the higher frequency components of the energy spectrum, which are expected to be affected by non-linear triad interactions. Furthermore, as depth-induced breaking models rely on a representative frequency of the energy spectrum (either f_p or f_{mean}), the model performances regarding the period should also be assessed. The overall model error is quantified with the Normalized Root Mean Square Error (NRMSE):

$$\mathrm{NRMSE}(X) = \sqrt{\frac{\sum_{i=1}^{N}(\hat{X}_i - X_i)^2}{\sum_{i=1}^{N} X_i^2}} \times 100 \tag{27}$$

where X and $\hat{X}$ respectively correspond to the vectors of measured and modelled bulk parameters of sample size N. In order to assess model performances for storm waves, the Normalized Bias (NB) and the NRMSE on H_{m0} are also computed on the 25% highest values. Assuming X and $\hat{X}$ stand for measured H_{m0} values sorted in ascending order and the corresponding model results, respectively. These indicators are given by:

$$\begin{cases} \mathrm{NB}_{3Q}(X) & = \frac{\sum_{i=3N/4}^{N}(\hat{X}_i - X_i)}{\sum_{i=3N/4}^{N} X_i} \times 100 \\ \mathrm{NRMSE}_{3Q}(X) & = \sqrt{\frac{\sum_{i=3N/4}^{N}(\hat{X}_i - X_i)^2}{\sum_{i=3N/4}^{N} X_i^2}} \times 100 \end{cases} \tag{28}$$

The resulting values presented in the following section are gathered in Tables 3 and 4.

4 Results

4.1 Wave forcing assessment

In nearshore application with barely no local wave growth due to weak local winds as during the two study cases considered here, wave transformation processes are mostly dissipative as the dominant source terms induce the dissipation of wave energy. Therefore it is essential to assess the wave forcing originating from WW3 application as it accounts for most of the energy income. For the case O10, WW3 results are assessed with offshore Biscay Buoy measurements (see Fig. 1a for its location). For the case D16, data from the Waverider buoy located inside the computational domain, in intermediate depth (17 m water depth), are used. There is an overall good agreement for each parameter as shown in Fig. 3. However, for the case D16, a strong underestimation of H_{m0}, T_{m02} and T_{pc} is noticeable after the peak of the storm around October the 10^{th}. The underestimation of H_{m0} reaches 0.9 m (25%) locally. As storm waves for the case D16 were produced by tropical hurricane Matthew, which passed only a few hundred kilometres from the study site, a small error on the storm track in the CFSR reanalysis could easily explain these larger errors but addressing this problem is outside the scope of the present study.

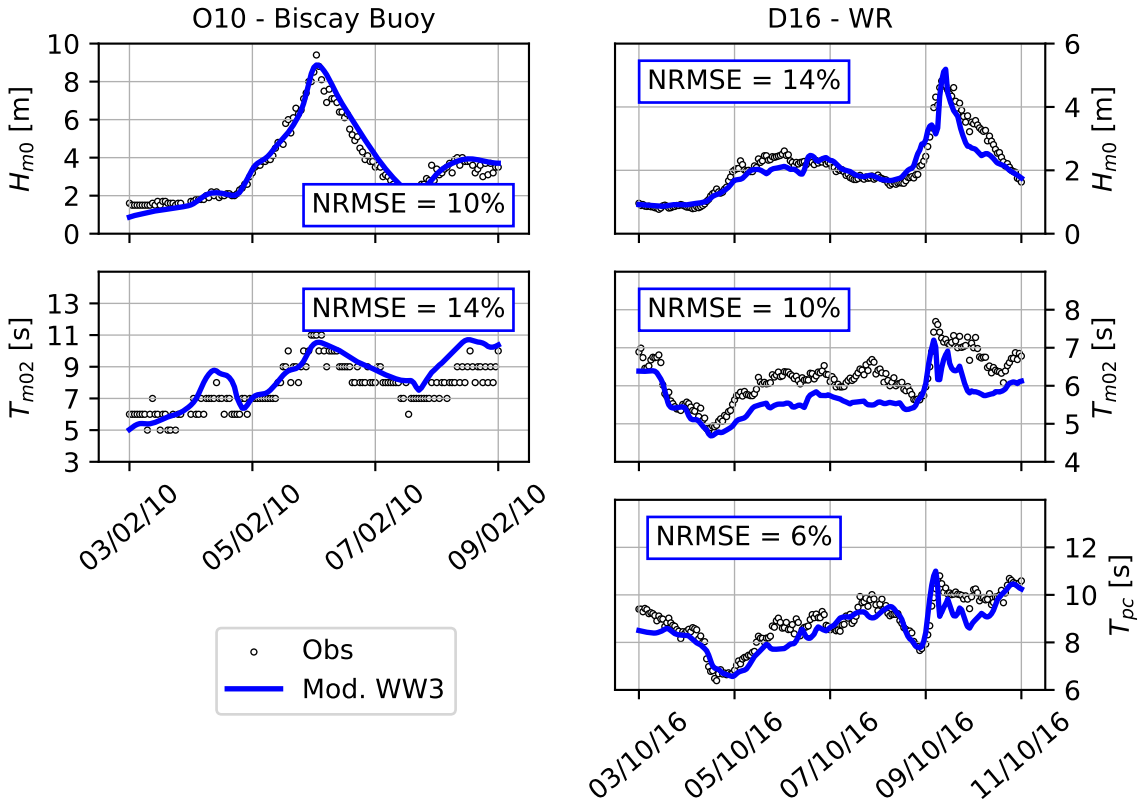

Figure 3: WW3/observations comparisons at the Biscay Buoy and at the Waverider buoy. There are no available measurements of the peak period (discrete or continuous) at Biscay Buoy.

4.2 Predictive skills of depth-induced breaking with default parameterizations

The four depth-induced breaking models presented above (namely BJ78, TG83, B98 and W10) were first tested on both study cases using their default parameterizations. The values assigned to the different parameters of depth-induced breaking formulations are recalled in Table 2. The results presented hereafter with TG83 formulation were obtained with the first weight function ($i = 0$ in Eq. 14) but the model showed similar behaviour using one or the other expression. It should be stressed that, as an initial approach, B is taken equal to unity in both TG83 and W10 models considering the lack of consensus for its optimal value (cf Sections 2.2.2 and 2.3.2).

BJ78	$\alpha = 1$; $\gamma = 0.73$
TG83	$B = 1$; $\gamma_{TG} = 0.42$; $i = 0$; $n_0 = 4$
B98	$\alpha = 1$; $\gamma = 0.73$
W10	$B = 1$; $\beta_{i,ref} = -4\pi/9$; $n = 2.5$; $\delta = 0.2$

Table 2: Depth-induced breaking formulations default parameters

4.2.1 Study case O10

Firstly, water levels are well reproduced by the model with a NRMSE on surface elevation around 15% at VEC and P3 locations (see Fig. 4j-k). The results on wave parameters strongly vary depending on the depth-induced breaking formulation used. With TG83 and W10 formulations, the results show a severe underestimation of wave energy at the peak of the storm which worsens closer to shore (Fig. 4b and 4c). The resulting NB_{3Q} on H_{m0} reaches respectively -33% and -36% at VEC location. Using the BJ78 formulation reduces the underestimation of H_{m0} across the instrumented profile during the storm peak, but it is still observable and NB_{3Q} reaches -12% at VEC location. The B98 formulation slightly improves the results obtained with BJ78

at each location. The underestimation of wave energy at the peak of the storm undermines the overall NRMSE on H_{m0} as shown in Tables 3 and 4. The results on wave periods are rather homogeneous, the NRMSE on T_{m02} varies between 10% and 16% depending on the location and the formulation used, whereas the NRMSE on T_{pc} approximately reaches 20% for each formulation.

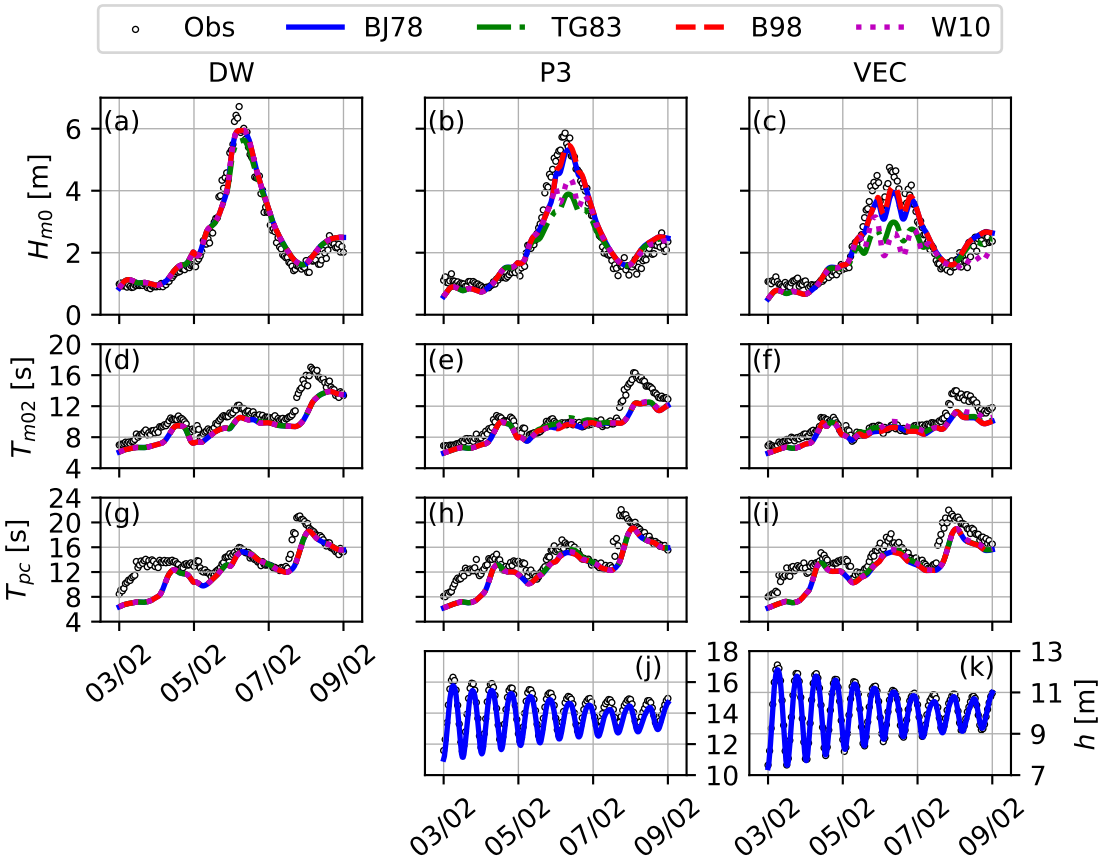

Figure 4: Measured and simulated H_{m0}, T_{m02}, T_{pc} and water depth (h) at the three measurement stations of the test case O10. For water depth timeseries, only one model output is being presented as similar results are obtained with the four models.

4.2.2 Study case D16

For the case D16, water levels are also fairly well reproduced (Fig. 5j-k), even though the uncertainty on the nominal bottom vertical location of the sensors undermines the NRMSE on surface elevation (16% at the ADOP location). For the four depth-induced breaking formulations tested here, the model results show a similar over-dissipation of energy at the storm peak as found in the O10 case (see Fig. 5a-c). When reaching the WR location, a considerable fraction of the incident wave energy has already been dissipated with the TG83 formulation at the storm peak in intermediate depth (Fig. 5a). The resulting NB_{3Q} on H_{m0} reaches -20%. At AS location, the results show an underestimation of H_{m0} at the peak of the storm for every models (Fig. 5b and Table 4). In shallower water, at the ADOP location, every formulations underestimate H_{m0} even before the storm peak (Fig. 5c): the NRMSE reaches 24%, 38%, 22% and 46% using BJ78, TG83, B98 and W10 formulations respectively. The over-dissipation of incident wave energy at the peak of the storm coincides with a slight overestimation of the mean wave period. The NRMSE on T_{m02} reaches 10% at the ADOP location with the W10 formulation.

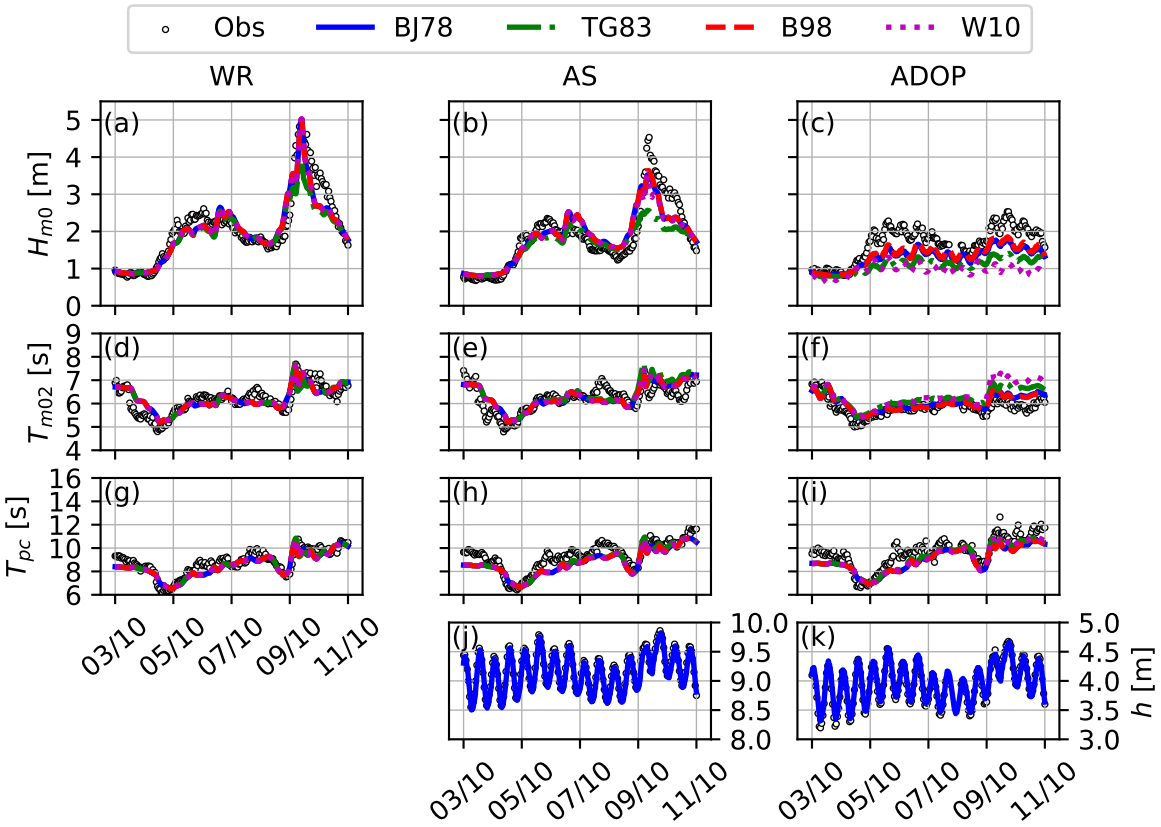

Figure 5: Measured and simulated H_{m0}, T_{m02}, T_{pc} and water depth (h) at the three measurement stations of the test case D16. For water depth timeseries, only one model output is being presented as similar results are obtained with the four models.

4.2.3 Adaptive parameterizations for γ and γ_{TG}

Several studies have pointed out the limitations of using a default parameterization in the BJ78 formulation. For instance, Groeneweg et al. (2009) reported an underestimation of the significant wave height and of the mean period in storm conditions in finite depth conditions. Further, for the TG83 formulation, it was stressed that the ratio H_{rms}/h in inner surf zones could vary with the beach morphology and with incident wave conditions (Sallenger Jr and Holman, 1985; Raubenheimer et al., 1996; Sénéchal et al., 2001). To address these limitations, several alternative parameterizations of the breaking index γ and γ_{TG} have been proposed to improve depth-induced breaking modelling with varying success (e.g., see Salmon et al., 2015, for a review).

Here, the model sensitivity to the breaking index γ for BJ78 and B98 models or γ_{TG} for TG83 model was investigated using the most landward sensor at both field sites. The parameter γ (respectively γ_{TG}) was tuned in order to match the H_{m0} observed at ADOP and VEC location (Fig. 6). These values considerably deviate from reference values (e.g. up to a factor 2 for γ_{TG}) and their expected range of variation (see for instance Salmon et al., 2015, and their Fig. 1). It is worth noting that opting for very large constant values to match the H_{m0} observed in the outer surf zone is not a reasonable solution as it will result in excessive wave height in the inner surf zone. For instance, Bertin et al. (2009) showed that the adequate breaking index in the inner surf zone at Oléron was 0.55 using BJ78 formulation. This tends to show the limitation of keeping γ (respectively γ_{TG}) constant. Furthermore, the results of this sensitivity test suggest that the local energy dissipation rate is not solely controlled by the parameterization of γ (respectively γ_{TG}), indirectly highlighting the role of the breaking coefficient, which is usually kept spatially constant around unity. Guérin et al. (2018) already introduced a scaled adaptive parameterization of the TG83 formulation for both γ_{TG} and B. These two parameters were computed as a linear function of the bottom slope adjusted to give the best fit of wave heights when comparing with measurements from a field campaign carried out in February 2017 in the shoreface of Oléron Island.

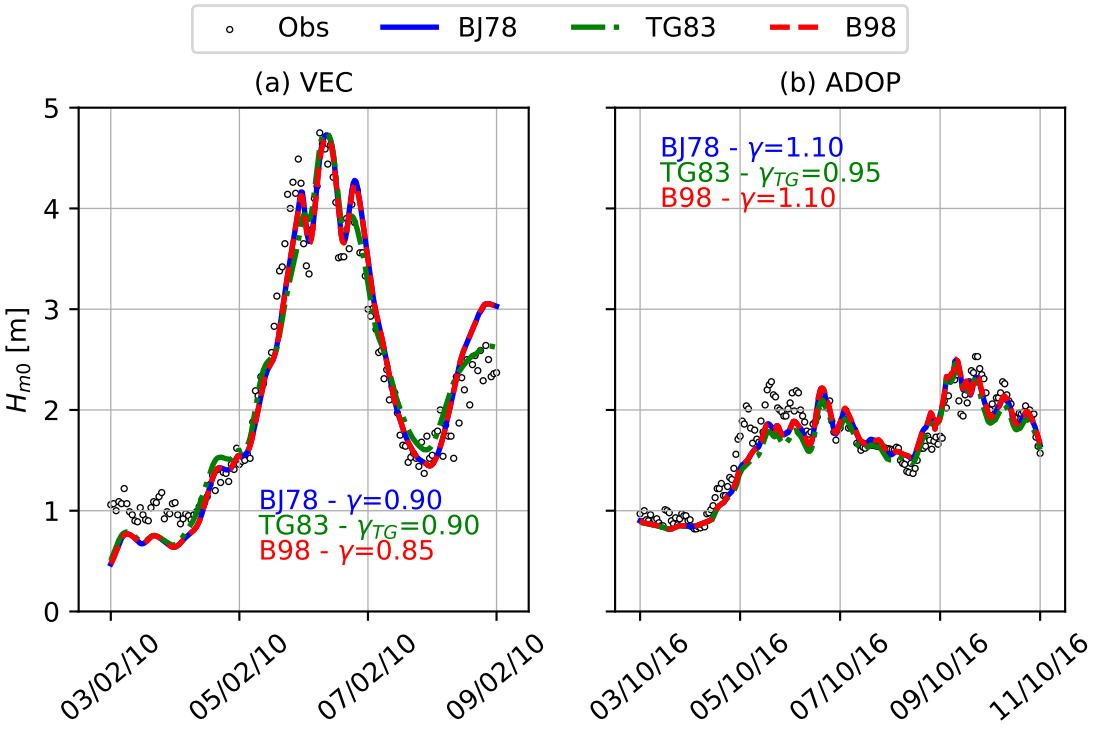

Figure 6: Measured and simulated H_{m0} at VEC (test case O10) and ADOP (test case D16) locations. Model results are issued from a tuned parameterization of the breaking index and γ_{TG} depending on the formulation used.

4.3 Role of the breaking coefficient

Despite the differences between BJ78/B98 models and TG83/W10 models, the rate at which energy is dissipated is formulated with the same bore-based approach, and is parameterized with the breaking coefficient. Consequently, the model performances using the adaptive parameterization of the breaking coefficient introduced in Eq. 6 are assessed. It should be stressed that the introduction of the adaptive breaking coefficient in BJ78 and B98 formulations would require a newly calibrated breaking index γ whereas, for TG83 and W10 models, the formulation of Q_b and its subsequent parameterization is based on observations collected in the surf zone or from laboratory experiments. Consequently, the model performances using either TG83/W10 or BJ78/B98 formulations with the adaptive parameterization of the breaking coefficient will be presented separately.

4.3.1 An adaptive breaking coefficient for TG83 and W10 formulations

For both study cases, the model was run again using TG83 and W10 formulations with B^3 substituted by B' whereas the other parameters were unchanged (see Table 2).

For the case O10, the adaptive parameterization of the breaking coefficient removes the observed underestimations obtained with TG83 and W10 formulations (Fig. 7a-c and Table 4). At the VEC location, the NRMSE is reduced to 12% and 15% with both formulations respectively. Yet, with the W10 formulation, an overestimation of H_{m0} is observed, with NB_{3Q} reaching 5%. The results on wave periods for both formulations are identical and remain very close to those obtained with the default parameterizations, hence these are not reproduced here (see Table 3). For the case D16, the adaptive parameterization leads to an overall reduction of the negative bias on H_{m0} and of the positive bias on T_{m02} such that the resulting timeseries approximately overlap at the WR and AS locations (only shown for H_{m0}, see Fig. 7d-e). The NRMSE on H_{m0} and T_{m02} are reduced at each location as shown in Table 3. However, the negative bias on H_{m0} at the ADOP location remains high using TG83 and W10 formulations, yielding a NRMSE on H_{m0} of 29% and 32% respectively.

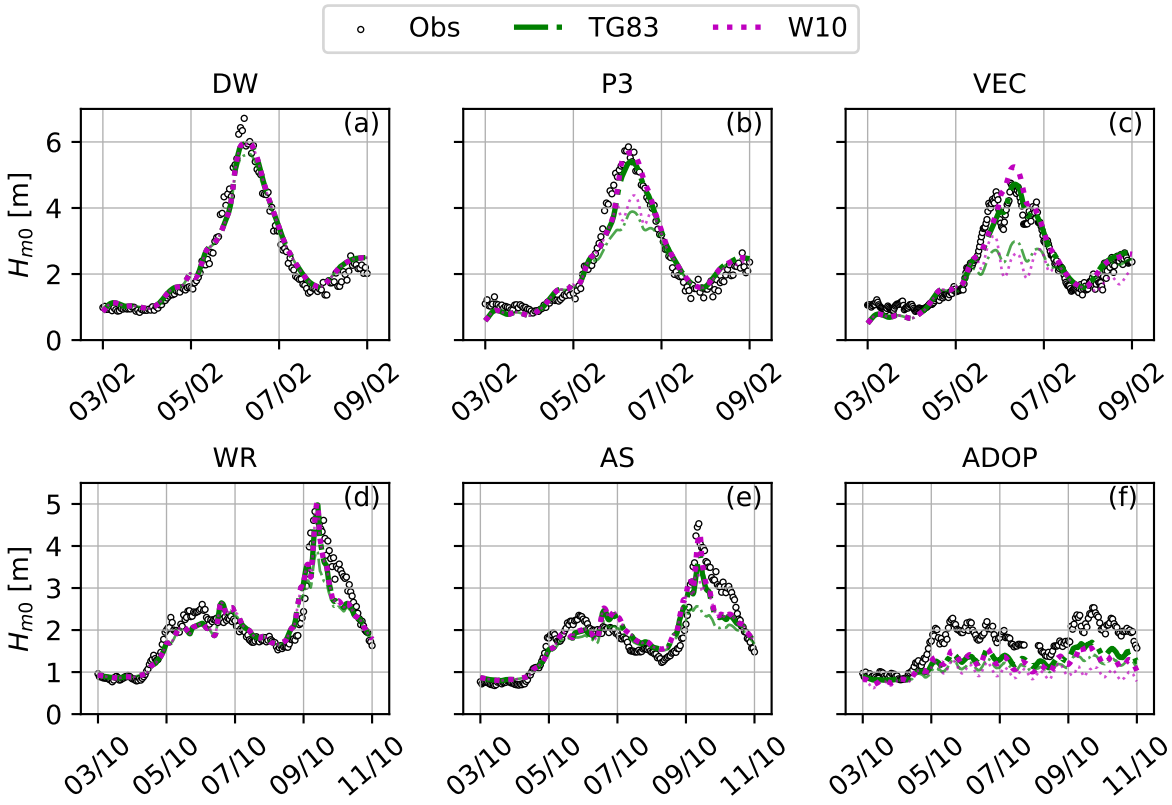

Figure 7: Measured and simulated H_{m0} for the two study cases using TG83 and W10 formulations with the adaptive parameterization of the breaking coefficient. The thin light curves correspond to the results obtained with the default parameterizations.

4.3.2 Toward a new parameterization of BJ78 and B98 formulations

For the BJ78 and B98 formulations, the introduction of the adaptive breaking coefficient leads the same formulations for the total energy dissipation rates (Eq. 10 and 16) with α substituted by B'. Furthermore, if the topography of the two study areas is rather similar, the study case O10 is characterized by higher peak periods (see Fig. 4g-i and 5g-i). Therefore the contrasted results between the two study cases could presumably be related to the different incident wave conditions. In order to investigate this hypothesis, the dependency of the breaking index to the local non dimensional water depth $k_p h$ was investigated following the approach of Ruessink et al. (2003). When the breaking coefficient is taken constant, the results are not improved with the parameterization of Ruessink et al. (2003) for the breaking index γ (not shown). Yet, the $k_p h$ dependency of γ is still expected to be valid with or without the adaptive breaking coefficient, such that this parameterization could also be tested with the adaptive breaking coefficient. Note, however, that the calibration performed by Ruessink et al. (2003) did not employ the present adaptive breaking coefficient so that different coefficients as those originally found by these authors might be expected. Nevertheless, finding an alternative calibration of the breaking index as defined in Eq. 17 falls outside the scope of the present study, therefore, the model was here run again with BJ78 and B98 formulations by taking into account the adaptive breaking coefficient and γ as obtained by Ruessink et al. (2003) and given in Eq. 17.

For the case O10, the new parameterization gives satisfactory results with the BJ78 formulation. The negative bias on H_{m0} at the storm peak resulting from the use of the default parameterization is corrected. However, the dissipation is underestimated with the B98 formulation, which results in an over-estimation of H_{m0} at VEC location (Fig. 8a-c and see Table 4). For the case D16, this parameterization reduces the negative bias on H_{m0} during the storm peak at AS location for both formulations (see Table 4). However, the bias on H_{m0} is still high at ADOP location (Fig. 8f) leading to a NRMSE which reaches 26% and 21% respectively.

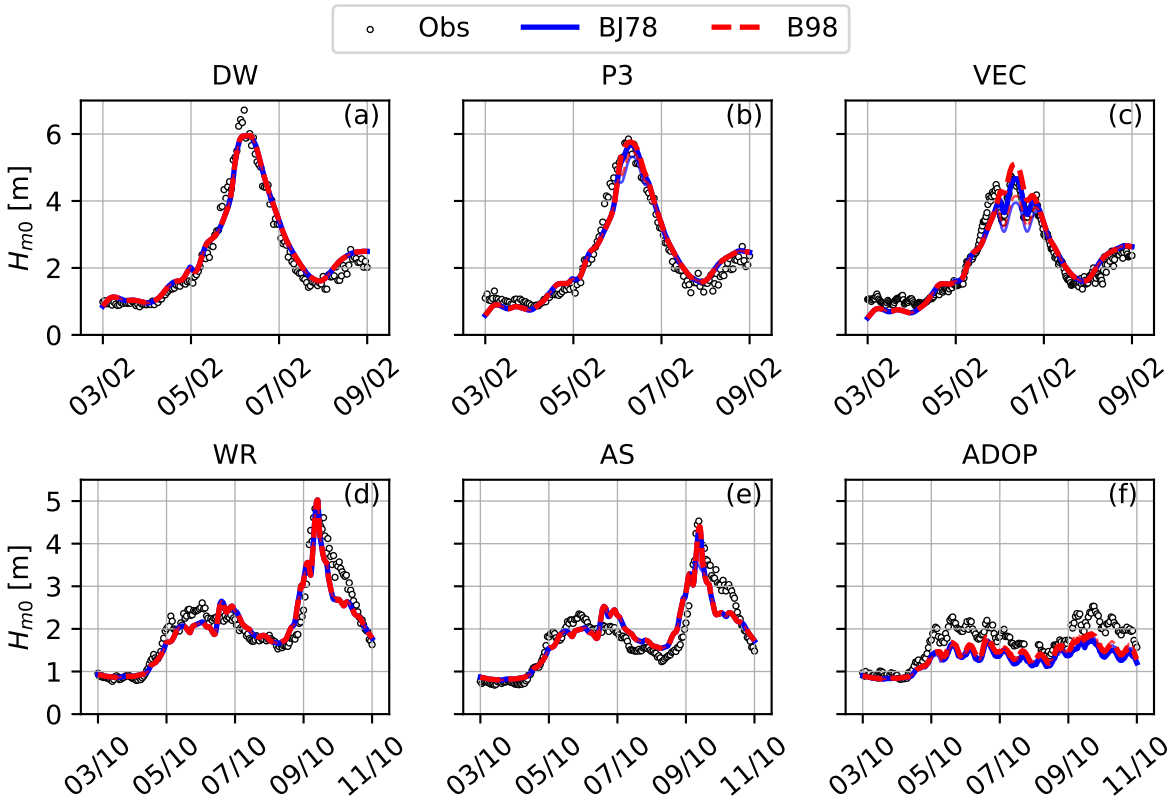

Figure 8: Measured and simulated H_{m0} for the two study cases using BJ78 and B98 formulations with the adaptive parameterization of the breaking coefficient. The thin light curves correspond to the results obtained with the default parameterizations.

		TG83		W10		BJ78		B98	
O10	DW								
	H_{m0}	11	**10**	10	10	10	10	10	10
	T_{m02}	16	16	16	16	16	16	16	16
	T_{pc}	20	20	20	20	20	20	20	20
	P3								
	H_{m0}	25	**12**	20	**11**	12	**11**	12	12
	T_{m02}	13	13	13	13	13	13	13	13
	T_{pc}	17	17	17	17	17	17	17	17
	VEC								
	H_{m0}	28	**12**	32	**15**	14	**11**	12	13
	T_{m02}	11	12	10	12	12	12	12	12
	T_{pc}	17	17	17	17	17	17	17	17
D16	WR								
	H_{m0}	18	**15**	15	15	15	15	15	15
	T_{m02}	6	6	6	6	6	6	6	6
	T_{pc}	6	6	6	6	6	6	6	6
	AS								
	H_{m0}	25	**18**	19	**17**	18	**17**	17	17
	T_{m02}	7	**6**	6	6	6	6	6	6
	T_{pc}	7	8	7	8	7	8	7	8
	ADOP								
	H_{m0}	38	**29**	46	**32**	24	26	22	**21**
	T_{m02}	8	**6**	10	**6**	5	5	5	5
	T_{pc}	8	8	8	9	9	9	9	9

Table 3: NRMSE (in %) at each location for the two study cases. For each formulation, the errors given in the first column were obtained with the default parameterizations whereas those given in the second column were obtained with the new parameterization. The bold values indicate whether better results are obtained with the new parameterization.

		TG83		W10		BJ78		B98	
O10	DW								
	NB_{3Q}	-5	**-1**	-1	-1	-1	-1	-1	-1
	$NRMSE_{3Q}$	9	**8**	8	8	8	8	8	8
	P3								
	NB_{3Q}	-26	**-6**	-18	**-2**	-7	**-3**	-5	**-2**
	$NRMSE_{3Q}$	28	**10**	21	**9**	11	**10**	10	10
	VEC								
	NB_{3Q}	-33	**-2**	-36	**5**	-12	**-2**	-9	**4**
	$NRMSE_{3Q}$	33	**10**	37	**15**	14	**9**	11	13
D16	WR								
	NB_{3Q}	-20	**-12**	-12	-12	-12	-12	-12	-12
	$NRMSE_{3Q}$	22	**16**	16	16	16	16	16	16
	AS								
	NB_{3Q}	-29	**-16**	-17	**-13**	-15	**-12**	-14	**-12**
	$NRMSE_{3Q}$	31	**18**	20	**16**	18	**16**	17	**16**
	ADOP								
	NB_{3Q}	-41	**-31**	-50	**-35**	-27	-29	-24	**-23**
	$NRMSE_{3Q}$	42	**31**	51	**35**	27	29	24	24

Table 4: $NB_{3Q}(H_{m0})$ and $NRMSE_{3Q}(H_{m0})$ (in %) at each location. For each formulation, the values given in the first column were obtained with the default parameterizations whereas those given in the second column were obtained with the new parameterization. The bold values indicate whether better results are obtained with the new parameterization.

5 Discussion

5.1 The origin of the over-dissipation obtained with default parameterizations

The results show an almost systematic over-dissipation of wave energy when using the default parameterizations of the four formulations for depth-induced breaking source terms. For both study cases, the relative importance of the energy dissipation rates due to wave breaking over all source terms was computed in order to get insight into the spatial variations and the local dominance of breaking processes. Variation rates corresponding to the source terms associated with the energy input from the wind (D_{in}) and the energy dissipation due to whitecapping (D_{ds}), bottom friction (D_{bf}) and depth-induced breaking (D_{br}) were extracted along a cross-shore profile (see Fig. 1b-c and 2b-c). The relative contribution of depth-induced breaking R_{br} was computed by normalising the associated dissipation rate by the quadratic sum of each source term:

$$R_{br} = \frac{|D_{br}|}{\sqrt{\sum D_j^2}} \text{ with } D_j = \int_{\sigma_{min}}^{\sigma_{max}} \int_0^{2\pi} \sigma S_j(\sigma,\theta) d\sigma d\theta \tag{29}$$

where the subscript j represents either of the 'in', 'ds', 'bf' or 'br' subscripts.

For the study case O10, wave breaking-induced energy dissipation modelled with the TG83 or W10 formulations is already substantial in intermediate depths (20 m and $k_p h \sim 0.6$), and it clearly dominates over any other dissipative processes (left panels of Fig. 9). Similar behaviour is observed for the BJ78 and B98 formulations closer to shore, slightly around P3 for the time displayed here (left panels of Fig. 9). At P3 location, a relatively strong divergence in terms of magnitude can be observed between the different formulations, with a maximum value of 75 W/m^2 reached with the W10 formulation while the TG83 formulation predicts a dissipation approximately three times weaker. For the case D16, the wave breaking-induced energy dissipation predicted by the TG83 formulation considerably differs from the other configurations. It shows a weak dissipation by depth-induced breaking all along the profile, even in intermediate depths ($k_p h \sim \mathcal{O}(1)$) which seemingly explains the

bias on H_{m0} at WR location (Fig. 5). In contrast, the other formulations produce a sharp transition regarding depth-induced breaking dominance (right panels of Fig. 9). Overall, it appears that TG83 model (and to a lesser extent W10 model) induces a substantial over-dissipation of wave energy for a wide range of $k_p h$ value, starting at intermediate depths where wave breaking due to interactions with the bottom is not expected. For the two other models, the results for study case O10 tend to show that the over-dissipation becomes substantial for $k_p h$ value of the order of 0.5, such conditions occur between AS and ADOP locations for study case D16.

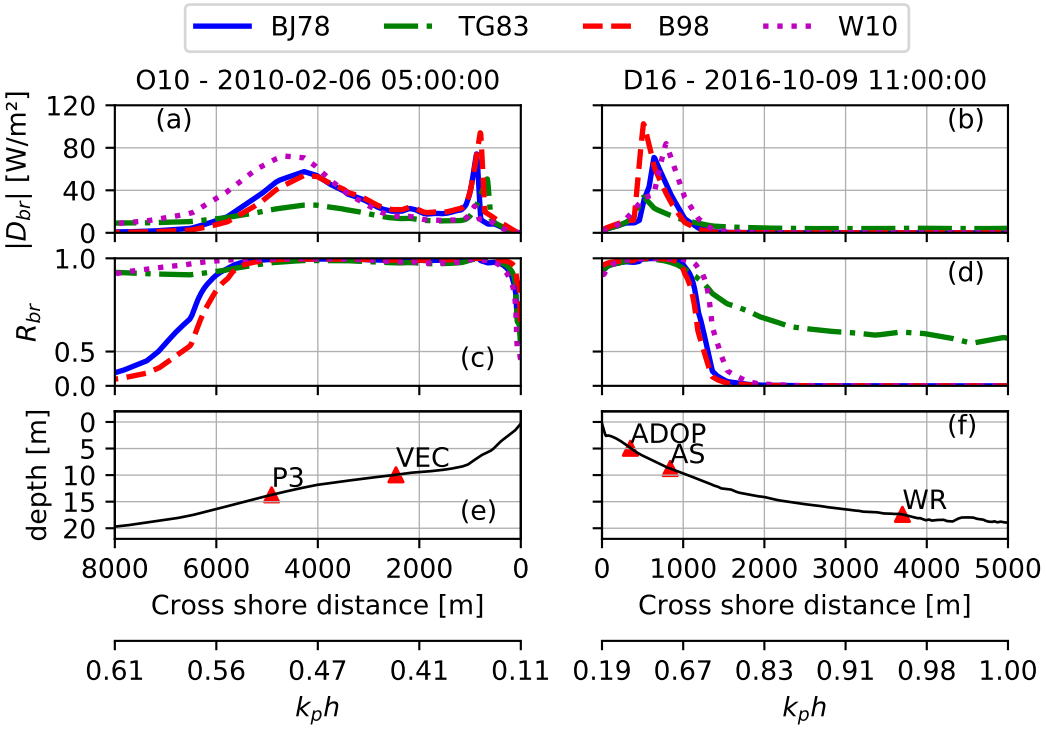

Figure 9: Energy dissipation rate profiles extracted during the storm peak associated to each study case (**a** and **b**) and associated normalised profiles (**c** and **d**). Depth, non-dimensional depth, and relative positions of measurement stations are given for reference (**e** and **f**).

The pragmatic solution proposed in this paper focuses on the role of the breaking coefficient in the formulation of the energy dissipation rate. The default parameterization of each formulation only considers saturated breakers whereas the adaptive breaking coefficient in these very gently-sloping shoreface area is $\mathcal{O}(0.1)$ which means that breakers are not saturated. Although the fraction of breaking waves is rather small and consequently the dissipation rates remain weak (see Fig. 9a-b), once integrated up to the inner surf zone, it results in a substantial dissipation of wave energy. Therefore, the difference of the energy dissipated by a saturated breaker and a non-saturated breaker explains the increasing over-dissipation of wave energy which results in an underestimation of significant wave heights in the nearshore area (Fig. 4a-c and 5a-c).

5.2 Remaining challenges

The accuracy of the total wave energy dissipation rate estimates strongly depends on the fraction of breaking waves Q_b, which remains a poorly understood quantity due to complications associated with its measurements and its natural variability (e.g., see Thornton and Guza, 1983; Stringari and Power, 2019; Martins et al., 2020).

On the one hand, for TG83 and W10 models, the formulation of Q_b and its subsequent parameterization rely on the fit of the observed fraction of breaking waves (using for instance video recording, e.g. Boers, 1996) to a local ratio constrained by the breaking process: either the $H_{rms}/\gamma_{TG}h$ ratio for TG83 formulation or the β/β_{ref} ratio for W10 formulation. For these two models the parameterization of Q_b depends both on the fitting coefficient (n) and on the aforementionned ratio (either through γ_{TG} or the value of β_{ref}). The parameterizations of Q_b could be improved by taking into account a wider range of wave conditions and topographies. For instance,

the reference biphase and the value of n in the weight function used for W10 model (Eq. 18) were fitted to data from only three cases from a laboratory experiment (see van der Westhuysen, 2010 and Boers, 1996). Furthermore, the model is particularly sensitive to the parameterization of the biphase: higher value for the parameter δ could be expected according to the alternative parameterization given by Doering and Bowen (1995). The model was tested with $\delta = 0.4$ to assess this sensibility in the present case. The corresponding results are shown Fig. 10 for the two study cases. Using $\delta = 0.4$ considerably improves the results for the D16 case, whereas, for the case O10, the beginning of the breaking is incorrectly predicted leading to an overestimation of significant wave heights. Although the biphase, being a third-order parameter, has potential for designing a robust breaking criterion standing on physical ground, more observations are probably required to improve its parameterization, especially through δ.

On the other hand, the BJ78 and B98 models rely on the same Miche type breaking criterion stating that a wave is breaking when its height exceeds some fraction of the local water depth given by the breaking index γ. For both models, the breaking index is the only parameter controling Q_b. It is rather questionable to ascertain a parameterization of such maximal wave height on the basis of observations outside a saturated surf zone. Consequently, the parameterization of the breaking index typically results from calibrations or inverse modelling approach (Ruessink et al., 2003). The counterpart is that the parameterization of the breaking index depends on the formulation used for the energy dissipation rate. An explanation of the overall satisfactory results using the default parameterizations of these two formulations would be that too high breaking index partly compensates the excessive saturated dissipation rate. Furthermore, it was shown that opting for a constant breaking index around its default value (or higher) could not give satisfactory results up to the inner surf zone where lower values are required (Bertin et al., 2009). Yet, the adaptive parameterization of the breaking coefficient introduced in this paper is more robust physically and should be explicitly taken into account in BJ78 and B98 formulations which, consequently, would require an adapted calibration of the breaking index.

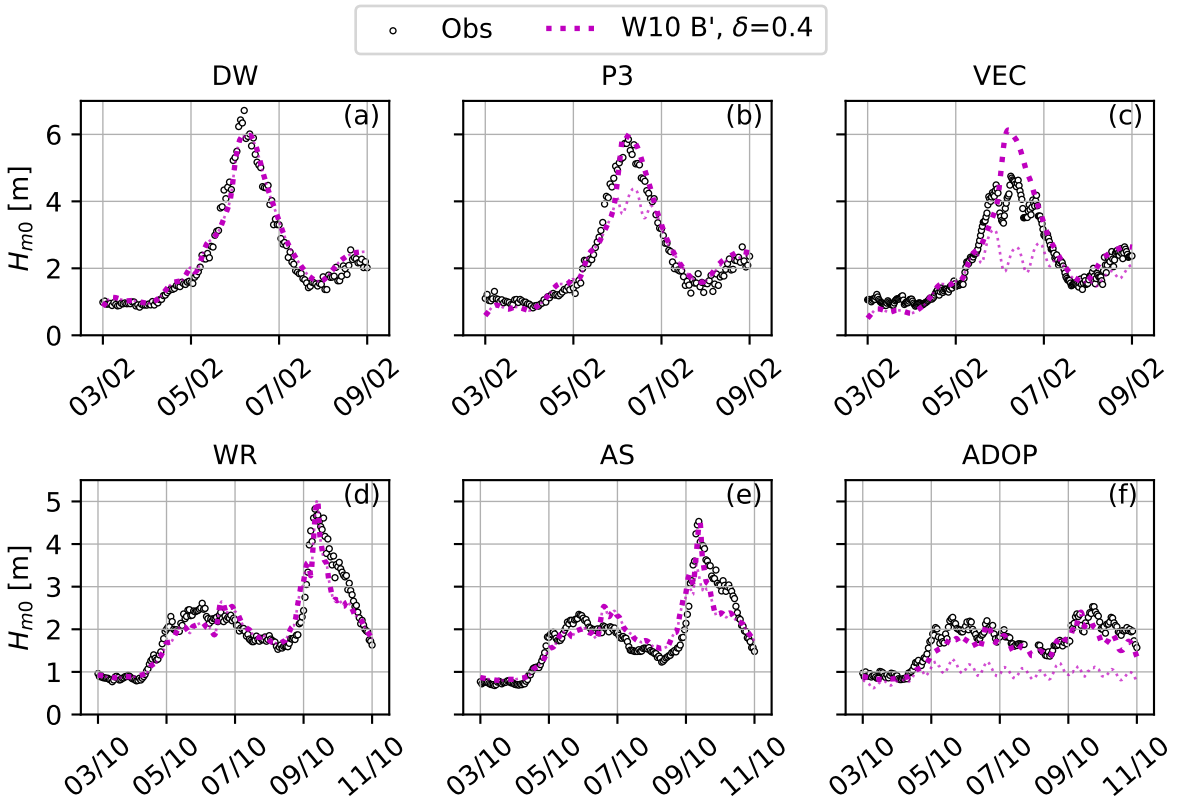

Figure 10: Measured and simulated H_{m0} for the two study cases using W10 formulation with a modified parameterization of the biphase. The thin light curves correspond to the results obtained with the default parameterization

It is worth noting that the pragmatic solution proposed in this study also faces the inherent limitations

of bore-based models. For instance, a number of field and laboratory observations have demonstrated that breaking processes have a certain inertia and keep being active as waves propagate in increasing water depths (e.g. behind bars or reefs, see Scott et al., 2005). The new parameterization of the breaking coefficient, as any other existing parameterization, does not account for such inertia processes. Surface roller models help representing these processes by slightly advecting the location where energy is actually dissipated towards the shoreline (e.g. Svendsen, 1984). For instance, the representation of surface rollers improve the predictions of longshore currents and their cross-shore structure in the presence of sandbars in the nearshore (Smith et al., 1993; Reniers and Battjes, 1997). Concerning the parameterization proposed in this study, it is best to maintain B' at a fixed level (e.g. ~ 0.1) over negative slopes. As both study cases do not present such topographic features, this solution could not be properly tested. In particular, this fixed value might show some site-specificity, and presumably needs adjustments.

5.3 Implications of this study

The accurate modelling of storm waves has a direct impact on the computation of the wave setup, which corresponds to the rise in mean water levels along the coast due to the forces exerted by short waves as they break. The setup is a key component of extreme water levels and thus play an important role in coastal hazards (e.g. Guérin et al., 2018). Considering an alongshore-uniform beach and neglecting the bottom stress, the depth-integrated momentum equation along a cross-shore transect simplifies to a balance between the cross-shore component of wave forces and the barotropic pressure gradient associated with the setup (e.g. Longuet-Higgins and Stewart, 1964):

$$\frac{\partial S_{xx}}{\partial x} + \rho g(\bar{\eta} + h)\frac{\partial \bar{\eta}}{\partial x} = 0 \tag{30}$$

where $\bar{\eta}$ corresponds to the sea surface elevation and S_{xx} is the cross-shore component of the radiation stress tensor, which, to first order, is a direct function of the total wave energy density. Salmon and Holthuijsen (2015) showed that inadequate depth-induced breaking parameterization could lead to a local underestimation of wave forces by up to a factor of 2. This study further suggests that an early wave energy dissipation in intermediate depth should result in weaker wave forces yielding an underestimation of wave setup near the shoreline. In order to verify this hypothesis, we compare hereafter the wave setup computed at the coast using an adaptive parameterization of the breaking coefficient to that obtained with the default parameterization. To account for various offshore wave conditions and topographies, Eq. 30 was coupled with a 1D cross-shore bulk wave model for a range of offshore wave conditions ($H_{rms,o}$ ranging from 2 to 12 m) and bottom slopes ($\tan\beta$ ranging from 1:10000 to 1:100). A corresponding peak period was computed from $H_{rms,o}$ by considering an empirical shape for the energy spectrum proposed by Pierson Jr and Moskowitz (1964). The resulting peak periods vary from 6 to 14.6 s. The wave energy dissipation by depth induced-breaking was modelled after BJ78 in which the maximal wave height is estimated through Eq. 8 with $\gamma = 0.73$. This parameterization is intended to be representative of the usual implementation of depth-induced breaking within spectral models for regional applications. The wave setup computed at the coast is systematically higher with the depth-induced breaking parameterized with the adaptive breaking coefficient (Fig. 11). The model clearly shows a reduced energy dissipation by depth-induced breaking for higher waves above gentle slopes when using the adaptive breaking coefficient such that the setup is uniform for given offshore wave conditions. Note that wave dissipation by bottom friction was neglected to focus on depth-induced breaking but could slightly change numbers presented in this discussion, particularly for the mildest slopes considered here. Nevertheless, this result tends to show that wave setup would be substantially underestimated when using depth-induced breaking default parameterization. The increase of the wave setup exceeds 100% for a wide range of offshore conditions above the most gentle slopes such that it could result in a setup up to 0.5 m higher (Fig. 11b-c). Over the last decade, the increase in computational power allowed accounting for the contribution of wave breaking to storm surges at regional scale (e.g., see Dietrich et al., 2011; Bertin et al., 2015; Wu et al., 2018). Yet, these studies presented wave setup contributions always lower than 1 m, even when considering wave height reaching $H_{rms} \sim 12$ m. As these studies typically employed the BJ78

model with default parameters, it is expected that these values are underestimated. It should be pointed out that previously published studies relying on 1D models (Raubenheimer et al., 1996; Apotsos et al., 2007) reported severe underestimations of wave setup along the coast. Guérin et al. (2018) proposed that this behaviour could be due to the wave-driven, depth varying circulation, not accounted for in depth-averaged approach of Eq 30. This numerical experiment tends to show that inadequate parameterization of depth-induced breaking could also result in a systematic underestimation of the wave setup under storm waves.

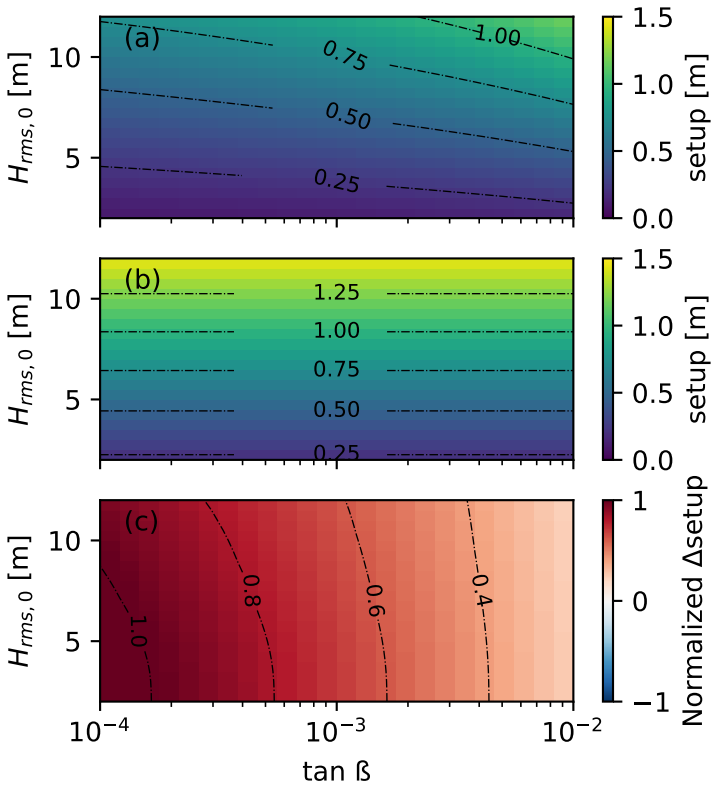

Figure 11: Wave setup computed at the position corresponding to the isobath 0 m for various wave incident conditions and bottom slopes with 1D model in which depth-induced breaking is modelled with BJ78 formulation by using the default parameterization **(a)** or the adaptive one **(b)**. The difference normalized by the default results is presented in the panel **(c)**.

6 Conclusions

In this study, the third generation spectral model WWM fully coupled with a 2DH configuration of the circulation model SCHISM was used to simulate nearshore dynamics under storm waves at two contrasting sites. The results show a substantial over-dissipation of wave energy by depth-induced breaking using four state-of-the-art formulations of the corresponding source terms. These results highlight the limitations of the default parameterization of the depth-induced breaking formulations. Alternatively, on the basis of earlier work by Le Mehauté (1962), an adaptive parameterization of the breaking coefficient is introduced and leads to improved predictions in the nearshore area. Yet, this solution will have to be verified in future studies, especially over topographies presenting negative slopes (e.g. barred beach), and combined with further calibration of the fraction of breaking waves in order to be valid up to the shoreline. Among the possible implications of this study, it is shown that the wave setup computed at the coast is significantly larger when using the adaptive parameterization for wave dissipation by breaking compared to that obtained with the default one.

Acknowledgements

M. Pezerat is supported by a PhD fellowship from CDA La Rochelle and from the FEDER project DURALIT. The study of extreme sea states and wave setup is a contribution to the Chair Regional Project EVEX. K. Martins acknowledges the financial support from the University of Bordeaux, through an International Postdoctoral Grant (Idex, nb. 1024R-5030). Authors greatly acknowledge the Hydrographic and Oceanographic French Office (SHOM) for providing field observations acquired during the projects MOUTON (funded by DGA PEA 012401) and EPIGRAM (funded by LEFE/IDAO and ANR, agreement ANR-08-BLAN-033001). Similarly, the acces to the experimental data at Duck made by the USACE is greatly appreciated.

A Adaptive breaking coefficient

Considering a one-dimensional situation where waves propagate over decreasing depth along the direction x, the energy flux balance entails that:

$$\frac{d(Ec)}{dx} = \frac{dE}{dt} \tag{A.1}$$

where E is the wave energy, c is the wave propagation speed. In the framework of solitary wave theory, it is shown that (Munk, 1949):

$$\frac{d(Ec)}{dx} = \frac{8}{3\sqrt{3}}\rho g \frac{d(H^{3/2}h^{3/2}c)}{dx} \text{ with } c = \sqrt{g(h+H)} \tag{A.2}$$

where h is the local water depth and H is the wave height. Furthermore, it is assumed that depth-induced breaking accounts for all of the energy dissipation. The energy dissipation rate per unit span is formulated according to Eq. 6 instead of Le Méhauté's original formulation. Therefore, Eq. A.1 reads:

$$\frac{8}{3\sqrt{3}}\rho g \frac{d(H^{3/2}h^{3/2}c)}{dx} = -\frac{B'}{4}\rho g H^3 \sqrt{\frac{g}{h}} \tag{A.3}$$

For solitary waves, a depth-limiting wave height is given by the McCowan's criterion $H_{max} = \tilde{\gamma}h$ with $\tilde{\gamma} = 0.78$ (Longuet-Higgins, 1974). Therefore, at the breaking point and inside the surf zone H is substituted with H_{max} such that, after some developments, Eq. A.3 gives:

$$\frac{dh}{dx} = -B'\frac{2}{7}\frac{3\sqrt{3}}{32}\frac{\tilde{\gamma}^{3/2}}{(1+\tilde{\gamma})^{1/2}} \Leftrightarrow B' \simeq 40\tan\beta \tag{A.4}$$

References

Andrews, D. G. and McIntyre, M. (1978). On wave-action and its relatives. *Journal of Fluid Mechanics*, 89(4):647–664.

Apotsos, A., Raubenheimer, B., Elgar, S., and Guza, R. (2008). Testing and calibrating parametric wave transformation models on natural beaches. *Coastal Engineering*, 55(3):224 – 235.

Apotsos, A., Raubenheimer, B., Elgar, S., Guza, R., and Smith, J. A. (2007). Effects of wave rollers and bottom stress on wave setup. *Journal of Geophysical Research: Oceans*, 112(C2).

Ardhuin, F., Rogers, E., Babanin, A. V., Filipot, J.-F., Magne, R., Roland, A., Van Der Westhuysen, A., Queffeulou, P., Lefevre, J.-M., Aouf, L., et al. (2010). Semiempirical dissipation source functions for ocean waves. part i: Definition, calibration, and validation. *Journal of Physical Oceanography*, 40(9):1917 – 1941.

Baldock, T., Holmes, P., Bunker, S., and Van Weert, P. (1998). Cross-shore hydrodynamics within an unsaturated surf zone. *Coastal Engineering*, 34(3-4):173 – 196.

Battjes, J. and Stive, M. (1985). Calibration and verification of a dissipation model for random breaking waves. *Journal of Geophysical Research: Oceans*, 90(C5):9159 – 9167.

Battjes, J. A. and Janssen, J. (1978). Energy loss and set-up due to breaking of random waves. In *Coastal Engineering 1978*, pages 569 – 587.

Battjes, J. A. and Janssen, T. T. (2009). Random wave breaking models-history and discussion. In *Coastal Engineering 2008: (In 5 Volumes)*, pages 25 – 37. World Scientific.

Bertin, X., Bruneau, N., Breilh, J.-F., Fortunato, A. B., and Karpytchev, M. (2012). Importance of wave age and resonance in storm surges: The case xynthia, bay of biscay. *Ocean Modelling*, 42:16 – 30.

Bertin, X., Li, K., Roland, A., and Bidlot, J.-R. (2015). The contribution of short-waves in storm surges: Two case studies in the bay of biscay. *Continental Shelf Research*, 96:1–15.

Bertin, X., Oliveira, A., and Fortunato, A. B. (2009). Simulating morphodynamics with unstructured grids: Description and validation of a modeling system for coastal applications. *Ocean modelling*, 28(1-3):75–87.

Bidlot, J.-R., Holmes, D. J., Wittmann, P. A., Lalbeharry, R., and Chen, H. S. (2002). Intercomparison of the performance of operational ocean wave forecasting systems with buoy data. *Weather and forecasting*, 17(2):287–310.

Bishop, C. T. and Donelan, M. A. (1987). Measuring waves with pressure transducers. *Coastal Engineering*, 11(4):309 – 328.

Boers, M. (1996). *Simulation of a Surf Zone with a Barred Beach: Wave heights and wave breaking*. Faculty of Civil Engineering, Delft University of Technology.

Booij, N., Ris, R. C., and Holthuijsen, L. H. (1999). A third-generation wave model for coastal regions: 1. model description and validation. *Journal of geophysical research: Oceans*, 104(C4):7649 – 7666.

Boudière, E., Maisondieu, C., Ardhuin, F., Accensi, M., Pineau-Guillou, L., and Lepesqueur, J. (2013). A suitable metocean hindcast database for the design of marine energy converters. *International Journal of Marine Energy*, 3:e40–e52.

Castelle, B., Marieu, V., Bujan, S., Splinter, K. D., Robinet, A., Sénéchal, N., and Ferreira, S. (2015). Impact of the winter 2013–2014 series of severe western europe storms on a double-barred sandy coast: Beach and dune erosion and megacusp embayments. *Geomorphology*, 238:135–148.

Cavaleri, L., Alves, J.-H., Ardhuin, F., Babanin, A., Banner, M., Belibassakis, K., Benoit, M., Donelan, M., Groeneweg, J., Herbers, T., Hwang, P., Janssen, P., Janssen, T., Lavrenov, I., Magne, R., Monbaliu, J., Onorato, M., Polnikov, V., Resio, D., Rogers, W., Sheremet, A., Smith, J. M., Tolman, H., van Vledder, G., Wolf, J., and Young, I. (2007). Wave modelling – the state of the art. *Progress in Oceanography*, 75(4):603–674.

Coco, G., Senechal, N., Rejas, A., Bryan, K. R., Capo, S., Parisot, J. P., Brown, J. A., and MacMahan, J. H. M. (2014). Beach response to a sequence of extreme storms. *Geomorphology*, 204:493 – 501.

Dietrich, J., Zijlema, M., Westerink, J., Holthuijsen, L., Dawson, C., Luettich Jr, R., Jensen, R., Smith, J., Stelling, G., and Stone, G. (2011). Modeling hurricane waves and storm surge using integrally-coupled, scalable computations. *Coastal Engineering*, 58(1):45 – 65.

Dodet, G., Bertin, X., Bouchette, F., Gravelle, M., Testut, L., and Wöppelmann, G. (2019). Characterization of sea-level variations along the metropolitan coasts of france: waves, tides, storm surges and long-term changes. *Journal of Coastal Research*, 88(sp1):10 – 24.

Doering, J. and Bowen, A. (1995). Parametrization of orbital velocity asymmetries of shoaling and breaking waves using bispectral analysis. *Coastal Engineering*, 26(1-2):15 – 33.

Eldeberky, Y. (1997). Nonlinear transformation of wave spectra in the nearshore zone. *Oceanographic Literature Review*, 4(44):297.

Eldeberky, Y. and Battjes, J. A. (1996). Spectral modeling of wave breaking: Application to boussinesq equations. *Journal of Geophysical Research: Oceans*, 101(C1):1253 – 1264.

Elgar, S. and Guza, R. T. (1985). Observations of bispectra of shoaling surface gravity waves. *Journal of Fluid Mechanics*, 161:425 – 448.

Filipot, J.-F. and Ardhuin, F. (2012). A unified spectral parameterization for wave breaking: From the deep ocean to the surf zone. *Journal of Geophysical Research: Oceans*, 117(C11).

Filipot, J.-F., Ardhuin, F., and Babanin, A. V. (2010). A unified deep-to-shallow water wave-breaking probability parameterization. *Journal of Geophysical Research: Oceans*, 115(C4).

Gallagher, E. L., Elgar, S., and Guza, R. T. (1998). Observations of sand bar evolution on a natural beach. *Journal of Geophysical Research: Oceans*, 103(C2):3203–3215.

Groeneweg, J., van der Westhuysen, A., van Vledder, G., Jacobse, S., Lansen, J., and van Dongeren, A. (2009). Wave modelling in a tidal inlet: Performance of swan in the wadden sea. In *Coastal Engineering 2008: (In 5 Volumes)*, pages 411 – 423. World Scientific.

Guérin, T., Bertin, X., Coulombier, T., and de Bakker, A. (2018). Impacts of wave-induced circulation in the surf zone on wave setup. *Ocean Modelling*, 123:86 – 97.

Hamm, L. (1995). *Modélisation numérique bidimensionnelle de la propagation de la houle dans la zone de déferlement*. PhD thesis, Université Joseph Fourier Grenoble 1.

Hamm, L. and Peronnard, C. (1997). Wave parameters in the nearshore: A clarification. *Coastal Engineering*, 32(2-3):119 – 135.

Hasselmann, K. (1962). On the non-linear energy transfer in a gravity-wave spectrum. Part 1. General theory. *Journal of Fluid Mechanics*, 12(4):481 – 500.

Hasselmann, K., Barnett, T., Bouws, E., Carlson, H., Cartwright, D., Enke, K., Ewing, J., Gienapp, H., Hasselmann, D., Kruseman, P., et al. (1973). Measurements of wind-wave growth and swell decay during the joint north sea wave project (jonswap). *Ergänzungsheft 8-12*.

Hasselmann, K., Munk, W., and MacDonald, G. (1963). Bispectra of ocean waves. In M. Rosenblatt (Editor), Time Series Analysis, pp. 125 – 139.

Hasselmann, S. and Hasselmann, K. (1985). Computations and parameterizations of the nonlinear energy transfer in a gravity-wave spectrum. part i: A new method for efficient computations of the exact nonlinear transfer integral. *Journal of Physical Oceanography*, 15(11):1369 – 1377.

Janssen, T. and Battjes, J. (2007). A note on wave energy dissipation over steep beaches. *Coastal Engineering*, 54(9):711 – 716.

Komen, G. J., Cavaleri, L., Donelan, M., Hasselmann, K., Hasselmann, S., and Janssen, P. A. E. M. (1994). *Dynamics and Modelling of Ocean Waves*. Cambridge University Press, Cambridge, U.K.

Le Mehauté, B. (1962). On non-saturated breakers and the wave run-up. *Coastal Engineering Proceedings*, 1(8):6.

Lin, S. and Sheng, J. (2017). Assessing the performance of wave breaking parameterizations in shallow waters in spectral wave models. *Ocean Modelling*, 120:41 – 59.

Longuet-Higgins, M. S. (1974). On the mass, momentum, energy and circulation of a solitary wave. *Proceedings of the Royal Society of London. A. Mathematical and Physical Sciences*, 337(1608):1 – 13.

Longuet-Higgins, M. S. and Stewart, R. (1964). Radiation stresses in water waves; a physical discussion, with applications. In *Deep sea research and oceanographic abstracts*, volume 11, pages 529 – 562. Elsevier.

Lubin, P. and Chanson, H. (2017). Are breaking waves, bores, surges and jumps the same flow? *Environmental Fluid Mechanics*, 17(1):47–77.

Martins, K., Blenkinsopp, C., Deigaard, R., and Power, H. E. (2018). Energy dissipation in the inner surf zone: New insights from li dar-based roller geometry measurements. *Journal of Geophysical Research: Oceans*, 123(5):3386–3407.

Martins, K., Bonneton, P., Mouragues, A., and Castelle, B. (2020). Non-hydrostatic, non-linear processes in the surf zone. *Journal of Geophysical Research: Oceans*, 125(2):e2019JC015521.

Miche, M. (1944). Mouvements ondulatoires de la mer en profondeur constante ou décroissante. *Annales de Ponts et Chaussées, 1944, pp (1) 26-78,(2) 270-292,(3) 369-406.*

Munk, W. H. (1949). The solitary wave theory and its application to surf problems. *Annals of the New York Academy of Sciences*, 51(3):376 – 424.

Nairn, R. B. (1990). *Prediction of cross-shore sediment transport and beach profiles evolution.* PhD thesis, Hydraulics Section - Department of Civil Engineering, Imperial College London.

Neumann, B., Vafeidis, A. T., Zimmermann, J., and Nicholls, R. J. (2015). Future coastal population growth and exposure to sea-level rise and coastal flooding-a global assessment. *PloS one*, 10(3):e0118571.

Nicolae-Lerma, A., Bulteau, T., Lecacheux, S., and Idier, D. (2015). Spatial variability of extreme wave height along the atlantic and channel french coast. *Ocean Engineering*, 97:175 – 185.

Owens, R. and Hewson, T. (2018). Ecmwf forecast user guide.

Pierson Jr, W. J. and Moskowitz, L. (1964). A proposed spectral form for fully developed wind seas based on the similarity theory of sa kitaigorodskii. *Journal of geophysical research*, 69(24):5181–5190.

Postacchini, M., Lalli, F., Memmola, F., Bruschi, A., Bellafiore, D., Lisi, I., Zitti, G., and Brocchini, M. (2019). A model chain approach for coastal inundation: Application to the bay of alghero. *Estuarine, Coastal and Shelf Science*, 219:56–70.

Raubenheimer, B., Guza, R., and Elgar, S. (1996). Wave transformation across the inner surf zone. *Journal of Geophysical Research: Oceans*, 101(C11):25589 – 25597.

Reniers, A. and Battjes, J. (1997). A laboratory study of longshore currents over barred and non-barred beaches. *Coastal Engineering*, 30(1-2):1–21.

Roelvink, J. and Stive, M. (1989). Bar-generating cross-shore flow mechanisms on a beach. *Journal of Geophysical Research: Oceans*, 94(C4):4785 – 4800.

Roland, A., Zhang, Y. J., Wang, H. V., Meng, Y., Teng, Y.-C., Maderich, V., Brovchenko, I., Dutour-Sikiric, M., and Zanke, U. (2012). A fully coupled 3d wave-current interaction model on unstructured grids. *Journal of Geophysical Research: Oceans*, 117(C11).

Ruessink, B., Walstra, D., and Southgate, H. (2003). Calibration and verification of a parametric wave model on barred beaches. *Coastal Engineering*, 48(3):139 – 149.

Saha, S., Moorthi, S., Wu, X., Wang, J., Nadiga, S., Tripp, P., Behringer, D., Hou, Y.-T., ya Chuang, H., Iredell, M., Ek, M., Meng, J., Yang, R., Mendez, M. P., van den Dool, H., Zhang, Q., Wang, W., Chen, M., and Becker, E. (2011). Ncep climate forecast system version 2 (cfsv2) selected hourly time-series products.

Sallenger Jr, A. H. and Holman, R. A. (1985). Wave energy saturation on a natural beach of variable slope. *Journal of Geophysical Research: Oceans*, 90(C6):11939 – 11944.

Salmon, J. and Holthuijsen, L. (2015). Modeling depth-induced wave breaking over complex coastal bathymetries. *Coastal Engineering*, 105:21–35.

Salmon, J., Holthuijsen, L., Zijlema, M., van Vledder, G. P., and Pietrzak, J. (2015). Scaling depth-induced wave-breaking in two-dimensional spectral wave models. *Ocean Modelling*, 87:30 – 47.

Scott, C. P., Cox, D. T., Maddux, T. B., and Long, J. W. (2005). Large-scale laboratory observations of turbulence on a fixed barred beach. *Measurement Science and Technology*, 16(10):1903.

Sénéchal, N., Dupuis, H., Bonneton, P., Howa, H., and Pedreros, R. (2001). Observation of irregular wave transformation in the surf zone over a gently sloping sandy beach on the french atlantic coastline. *Oceanologica Acta*, 24(6):545 – 556.

Smith, J. M. (2002). Wave pressure gauge analysis with current. *Journal of waterway, port, coastal, and ocean engineering*, 128(6):271–275.

Smith, J. M., Larson, M., and Kraus, N. C. (1993). Longshore current on a barred beach: Field measurements and calculation. *Journal of Geophysical Research: Oceans*, 98(C12):22717–22731.

Stoker, J. J. (1957). Water waves: the mathematical theory with applications.

Stringari, C. E. and Power, H. E. (2019). The fraction of broken waves in natural surf zones. *Journal of Geophysical Research: Oceans*, 124(12):9114–9140.

Svendsen, I. A. (1984). Wave heights and set-up in a surf zone. *Coastal engineering*, 8(4):303–329.

The Wamdi Group (1988). The wam model – a third generation ocean wave prediction model. *Journal of Physical Oceanography*, 18(12):1775–1810.

Thornton, E. B. and Guza, R. (1982). Energy saturation and phase speeds measured on a natural beach. *Journal of Geophysical Research: Oceans*, 87(C12):9499–9508.

Thornton, E. B. and Guza, R. (1983). Transformation of wave height distribution. *Journal of Geophysical Research: Oceans*, 88(C10):5925 – 5938.

Tolman, H. L. (1991). A third-generation model for wind waves on slowly varying, unsteady, and inhomogeneous depths and currents. *Journal of Physical Oceanography*, 21(6):782 – 797.

van der Westhuysen, A. J. (2010). Modeling of depth-induced wave breaking under finite depth wave growth conditions. *Journal of Geophysical Research: Oceans*, 115(C1).

Willebrand, J. (1975). Energy transport in a nonlinear and inhomogeneous random gravity wave field. *Journal of Fluid Mechanics*, 70(1):113–126.

Wright, L. D. and Short, A. D. (1984). Morphodynamic variability of surf zones and beaches: A synthesis. *Marine Geology*, 56(1):93 – 118.

Wu, G., Shi, F., Kirby, J. T., Liang, B., and Shi, J. (2018). Modeling wave effects on storm surge and coastal inundation. *Coastal Engineering*, 140:371 – 382.

Zhang, Y. J., Ye, F., Stanev, E. V., and Grashorn, S. (2016). Seamless cross-scale modeling with schism. *Ocean Modelling*, 102:64 – 81.